ICFO-INSTITUT DE CIÈNCIES FOTÒNIQUES
&
UPC-UNIVERSITAT POLITÈCNICA DE CATALUNYA

Optical surfaces for mid-infrared sensing

Kavitha Kalavoor Gopalan

Thesis advisor: Prof. Valerio Pruneri

PhD Thesis - 2018

To Amma, Achan and Kannan
...for their unconditional love, trust and support.

&

To Deepu
...for helping me believe that there is always light at the end of the tunnel.

Abstract

The mid-infrared (mid-IR) spectral region, with wavelengths between 3 and 15 μm, is known for a wide range of applications ranging from spectroscopic sensing to thermal imaging. However, despite the strong technological interest, optoelectronic devices in the mid-IR are expensive and often inferior in performance compared to their visible and near-IR counterparts. In this thesis, we combine ultrathin materials, e.g. graphene, and novel substrates to develop optical surfaces for applications in the mid-IR.

First, we demonstrate a novel uncooled photodetector, combining graphene with a ferroelectric (pyroelectric) substrate. More specifically, we develop a graphene on z-cut lithium niobate ($LiNbO_3$) pyro-resistive platform that supports dynamic tunablity of the responsivity. We also develop a model to identify the key parameters that influence the performance of such detectors and can therefore provide guidelines to improve their performance.

Second, we introduce ultra-thin yttria-stabilized zirconia (YSZ), a ceramic material, as a novel platform for IR nano-optics. In particular, we combine YSZ substrates with metallic nanostructures and graphene to demonstrate plasmonic, polarizing and transparent heating devices, which enable high temperature processing and can withstand harsh environments thanks to the high thermal and chemical stabilities of YSZ. Additionally, the mechanical flexibility of YSZ substrates also makes them ideally suited for manufacturing foldable or bendable devices and for low cost large-scale roll-to-roll fabrication processes.

Finally, we investigate for the first time electrostatically tunable graphene nanohole array surfaces by performing a detailed experimental study of structures with periods as low as 100 nm. We obtain a clear plasmonic response

from these surfaces in the range 1300-1600 cm^{-1}. We also demonstrated for the first time that these tunable nanostructures can be fabricated by scalable nano-imprint technique. Such large area plasmonic nanostructures are suitable for industrial applications, for example, surface-enhanced infrared absorption (SEIRA) sensing. This is because they combine an easy design, extreme field confinement and the possibility to excite multiple plasmon modes for multi-band sensing, a feature not readily available in nanoribbons or other localized resonant geometries.

The results contained in this thesis are particularly relevant with regard to extending the use of materials, such as graphene combined with specific substrates ($LiNbO_3$ or zirconia), to mid-IR photodetection, enhanced absorption and molecular sensing.

Resumen

La región espectral del infrarrojo medio (mid-IR), de longitudes de onda entre los 3 y los 15 μm, se conoce por su vasto número de aplicaciones: desde la detección espectroscópica hasta la imagen térmica. No obstante, a pesar de su gran interés tecnológico, los dispositivos optoelectrónicos en el mid-IR son caros y, a menudo, con rendimientos inferiores al compararlos con sus homólogos en la región visible y en el infrarrojo cercano. En esta tesis, combinamos materiales ultrafinos (e.g. grafeno) con nuevos substratos para desarrollar superficies ópticas con aplicaciones en el mid-IR.

Primero, mostramos los resultados de un fotodetector innovador, que no necesita ser enfriado, fabricado combinando grafeno con un substrato ferroeléctrico (piroeléctrico). Más específicamente, desarrollamos un artefacto de grafeno dispuesto sobre niobato de litio ($LiNbO_3$) cortado en la dirección z, que admite una modulación dinámica de su capacidad de respuesta. También desarrollamos un modelo matemático con el propósito de identificar los parámetros claves que influyen en el rendimiento de estos fotodetectores y, en consecuencia, proporcionar una serie de pautas para mejorarlo.

En segundo lugar, introducimos la circonita estabilizada con óxido de itrio ultrafina (YSZ) como material cerámico vanguardista en el campo de la nanoóptica en el IR. En particular, combinamos substratos de YSZ con nanoestructuras metálicas y grafeno para demostrar la idoneidad de dispositivos plasmónicos, transparentes y polarizadores, que posibilitan el procesamiento a alta temperatura y que pueden soportar condiciones ambientales más duras gracias a la excelente estabilidad térmica y química de la YSZ. Además, la flexibilidad de los substratos de YSZ hace de éstas, unas estructuras ideales para la manufac-

tura de dispositivos flexibles y plegables, cuyo proceso rollo-a-rollo de fabricación a gran escala es de bajo coste.

Finalmente, investigamos por vez primera las superficies de grafeno moduladas electrostáticamente con patrones de nano-orificios, cuyos periodos llegan a distancias tan pequeñas como los 100 nm, por medio de un exhaustivo estudio experimental. A través del mismo, obtenemos una respuesta plasmónica clara en el rango de los 1300-1600 cm^{-1}. También demostramos por primera vez, que estas nanoestrucutras modulables pueden ser fabricadas mediante técnicas escalables de nanoimpresión. Las grandes dimensiones de dichas nanoestructuras plasmónicas, las hacen plenamente apropiadas para aplicaciones industriales como, por ejemplo, la detección por absorción infrarroja amplificada de superficie (SEIRA, por sus siglas en inglés). Esto ocurre debido a que combinan un diseño simple, con un confinamiento extremo del campo y con la posibilidad de excitar diferentes modos plasmónicos, lo que es de gran utilidad para la detección multi-banda, una característica difícil de conseguir con cintas de grafeno u otras geometrías localizadas resonantes. Los resultados integrados en esta tesis son particularmente relevantes con respecto a la extensión de la utilización de materiales como el grafeno en combinación con substratos específicos ($LiNbO_3$ o circonita) para la fotodetección en el mir-IR, la absorción amplificada y la detección molecular.

This thesis was financially supported by the International PhD fellowship program "la Caixa"-Severo Ochoa @ ICFO.

Acknowledgements

This section is an attempt to awaken my *inner Shakespeare* to thank all the people who have made this journey special and fruitful.

I will be forever indebted to this warm country and its equally warm people who made it a privilege to call it home for more than 4 years.

I would like to express my gratitude to my thesis supervisor Valerio for giving me the opportunity to join his wonderful Opto-group. It has been an incredible learning experience with him and the amazing team that he always manages to hire. In spite of his busy schedule, multiple students and projects, he has always made time for each one of us. A good amount of results described in this thesis originate from his 'Friday-afternoon-experiment' ideas (which most often did not end on a Friday afternoon). Despite his best efforts to not show it, Valerio has been one of the most understanding and considerate professors I have known.

I am thankful to the committee members for their valuable advices to improve this thesis.

Thanks to the ICFO HR- Manuela, Cristina, Mery for their excellent job and making life easier for foreign students like me. I am indebted to Anne, who was the first contact person at ICFO, for her very affectionate gestures and organizing many hikes and trips.

Thanks to Luis and Javi for keeping the nanofabrication lab, where I have spent countless hours making (and sometimes breaking) things, up and always running. I am also grateful to Johann for his helpful lithography tips and for lending some chemicals.

Thanks to Jose Carlos, Xavi and everyone at the electronic and mechanical

workshops and IT for making research at ICFO a lot easier.

Thanks to the ICFO front desk for letting me in with a smile, all those times that I forgot my card. I am thankful to the ICFO purchasing, travel and logistics for doing their functions exceptionally well.

I am grateful to my first post-doc/mentor Davide, with whom I did my very first fabrication and experiments for the PhD. In addition to a lot of physics and problem solving, I also learned many Italian 'keywords' from him. He also helped me deal with a lot of self-doubt that most first year PhDs deal with.

Thanks to Dani for sharing his contagious passion and perfectionism in everything that he takes up. It was a great privilege to learn about graphene plasmonics from you.

Thanks to my current super-post-doc Bruno for giving his best at answering the silliest of my questions with great patience. I owe him a lot for helping me give this thesis its flow and outline.

Thanks to Vittoria, without whom half of my experiments would not have been set up as easily. I really admire the commitment with which she helps each one of us.

I would also like to thank Lisa Ruby for patiently proof reading this thesis.

I thank Prof. Frank Koppens for giving me access to his labs and introducing me to his group members for the experiments in Chapter 3. Seb and Romain, thank you for helping me through the mid-infrared measurements and for the coffee and conversations in between. I am also grateful to David Alcaraz for always lending me a hand and fixing things for me during my experiments at Frank´s lab. The very talented Fabien Vialla also deserves my gratitude for making the beautiful graphics for figure 3.6.

Thanks to David from DTU for the samples that were crucial for the experiments in Chapter-5.

On days that my experiments did not work, my Office -257 has always managed to cheer me up with random conversations. Roland has been a very good accomplice at everything and it is with him that I have hopes to take over the world, but before that, we need to learn how to clean those polarizers. Thanks to Alican for being a really great friend and pushing me to do my first 10k and triathlon. As promised, all the graphs in this thesis are color blind proof, just for you! I genuinely appreciate the company of Josselin, who always

has the most interesting sweets and anecdotes from China and knows the best ways to phrase tactful emails. Thanks to Luc for being almost like an elder brother and the constant supply of Swiss chocolates and life/PhD advices. We are by far the best office in the history of offices.

Miriam, my graphene soulmate as she likes to put it, has been the best person to complain (cry) to about broken graphene samples and failed experiments.

Thanks to the cleanroom friends who helped survive those long (freezing) waiting hours.

I am thankful to the ever-growing Opto-familia: Rafael, Juan Miguel, Juan R, Waldo, Carlos, Rubi, Raju, Xanna, Robin, Cedric, Fabi, Nestor and many others for some great conversations and friendship.

I feel extremely fortunate to have made friends that have set the bar very high for my future friends. To (my Blondie) Pamina, for starting that conversation at the Tarragona hike and her unparalleled friendship and hugs ever since. I will always be in awe of how you care for people and know the best ways to make them feel special. To Sandra, for convincing me to do crazy things (including the triathlon that I am currently recovering from) and being my saviour at insane hours. You are one of the strongest (not referring to your 6-pack here) and nicest human beings that I will ever meet. The spontaneous trips, beach walks and café de finca conversations with you girls have been some of the best times of the last 4 years.

Thanks to Irene for sharing our amazing home and inspiring me to start the journey towards the fitter version of myself.

Some long working days that turned into working nights and working weekends were enjoyable only because of the company of Rinu, who manages to brighten up the grumpiest of people with his trademark smile and kindness.

Thanks to Anuja for her (friendship and) Indian snacks collection which has fed me during some long days at ICFO. To Susmita, for sharing my love for food, some great trips and inside jokes. To Vindhiya, for the jokes, food and conversations that only South Indians get. To my junior, Vikas for keeping some college memories alive and giving all of us some very good reasons to laugh. Huge thanks to my other Castefa people Ugaitz, Julio, Iker, Alvaro (extra points for the chocolates) for making life in Castelldefels more fun than

ever. To many friends from ICFO and outside :Lisa, Inci, Jordi, Tanja, Senaida, Ozlem, Shahrzad, Hugo for all the fun we had.

I feel extremely blessed to have school friends like Ayisha, Achu and Bhagya cheering for me from miles away. To my childhood friend, Swathi for convincing me that I am not as stupid as I think, since primary school. To my college friend, Zarin for always understanding how I felt and giving some good advices.

I also acknowledge the teachers from school and college who have laid the foundation for this journey. I would especially like to thank my favorite teacher from school,Vijayakumar sir, for his support and encouragement.

Thanks to my extended family- aunts, uncles and cousins for always wishing the best for me.

Thanks to my boyfriend Deepak, for literally being the better-half in this relationship-for transforming my complaints into smiles and having the solutions to some equations and problems that I didn´t want to face. I am so proud of us for making it this far despite the distance and all odds. I am also grateful to his supportive parents who welcomed me into their family with open arms.

'Thank you' is too little a word to express my gratitude to my ever loving and supportive family. My father, Gopalan has been my greatest source of inspiration. My mother, Kamala has always been the first one to remind me to be humble and grateful; which is probably the reason for my long acknowledgement section. My brother, Navaneeth (Kannan) has stood by me and for me, while I made many of my life decisions. All dreams that I chase and fulfill, including this PhD, equally belong to them.

"It's what you learn after you know it all, that counts." - John Wooden

List of publications

List of publications included in this thesis

1. Mid-infrared pyroresistive graphene detector on $LiNbO_3$.
   K. K. Gopalan, D. Janner, S. Nanot, R. Parret, M. B. Lundeberg, F. H. L. Koppens, V. Pruneri, Advanced Optical Materials, 5, 1600723 (2017).

2. Scalable and tunable periodic graphene nanohole arrays for mid-infrared plasmonics.
   K. K. Gopalan, B.Paulillo, D.M.A.Mackenzie, D.Rodrigo, Nestor Bareza, P.R.Whelan, A.Shivayogimath, V.Pruneri, Nano Letters,, Article ASAP, Online DOI: 10.1021/acs.nanolett.8b02613] (2018)

3. Ultra-thin yttria-stabilized zirconia as a flexible and stable substrate for infrared nano-optics.
   K.K. Gopalan, D. Rodrigo, B. Paulillo, K.K. Soni, V. Pruneri, Advanced Optical Materials, under review.

Other publications from the author not included in this thesis:

1. Tunable complete optical absorption in multilayer structures including $Ge_2Sb_2Te_5$ without lithographic patterns.
   V. K. Mkhitaryan, D. S. Ghosh, M. Rudé, J. Canet-Ferrer, R. A. Maniyara, K. K. Gopalan, V. Pruneri, Advanced Optical Materials, 5, 1600452 (2016).

Conference presentations:

1. Ultrathin metals and graphene for flexible optoelectronic devices.
   M. Marchena, T. L. Chen, K. Kalavoor, D. Janner, D. S. Gosh, V. Pruneri
   Trends in Nanotechnology International Conference (TNT2014), Barcelona, Spain, October 2014

2. Pyroresistive infrared detector using graphene on $LiNbO_3$.
   D. Janner, K. Kalavoor, S. Nanot, R. Parret, F. Koppens, V. Pruneri
   Graphene, Genova, Italy, April .

3. Graphene for transparent conductors and infrared sensing.
   K. K. Gopalan, M. Marchena, J. Rombaut, I. Gris, D. Rodrigo, V. Pruneri
   CLEO-PR, OECC PGC, Singapore, July-August, 2017.

4. Multifunctional nano-structured optical surfaces for industrial applications.
   M. A. Noyan, K. K. Gopalan, R. A. Maniyara, M. M. Martin-Frances, V. Mkhitaryan, J. Rombaut Segarra, M. Rude, R. Sibilo, I. Mannelli, J. Canet Ferrer, V. Pruneri
   Nanometa 2017, Seefeld, Austria, January 2017.

5. Mid-infrared photo detector using pyroelectric response of $LiNbO_3$.
   K. K. Gopalan, D. Janner, S. Nanot, R. Parret, M. B. Lundeberg, F. H. L. Koppens, V. Pruneri
   SPIE Optical Engineering + Applications, San Diego, USA, August 2017.

6. Mid-infrared photo detector using pyroelectric response of $LiNbO_3$.
   K. K. Gopalan, D. Janner, S. Nanot, R. Parret, M. B. Lundeberg, F. H. L. Koppens, V. Pruneri
   Nanophotonics of 2D materials (N2D), San Sebastián, Spain, July-August 2017

Contents

List of Figures

Chapter 1

Introduction

The mid-infrared (mid-IR) (3-15 μm) spectral region is of great scientific and technological interest. It is home to strong characteristic vibrational transitions of many important molecules such as proteins and other biomolecules, which makes it relevant for applications such as spectroscopy, material processing, and chemical and bio-molecular sensing. Furthermore, two atmospheric transmission windows (3-5 μm and 8-13 μm) also lie in the mid-IR, this being crucial for remote detection of explosive gases and thermal imaging. Thus, there is intense ongoing research towards the development of mid-IR optoelectronics. However, unlike the visible and near-infrared regions of the spectrum, optoelectronic devices in the mid-IR are expensive and often inferior in performance [1, 3]. For example: (i) photodetectors in the mid-IR are expensive and often require cryogenic cooling to operate; (ii) spectroscopy in the mid-IR is challenging because of the size mismatch between the wavelength of the light and the absorption cross sections of the target molecules; (iii) the presence of the numerous phonon bands make it difficult to find substrates that are transparent in the mid-IR, for use in applications like spectroscopy and IR windows. Therefore, there is extensive effort in investigating materials and their combinations that will make mid-IR technologies viable.

The overall objective of this thesis is to combine ultrathin materials, like graphene, and novel substrates to develop surfaces for application such as pho-

todetection, enhanced absorption and molecular sensing in the mid-IR.

The thesis is organised in the following chapters:

Chapter 2 provides a general overview of the current technologies and challenges in the mid-IR. It also sheds light on the relevant material properties and underlying physics. The purpose of this chapter is to set the stage for the following chapters where we explore and implement various technologies for use in the mid-IR.

In Chapter 3, we describe a novel uncooled mid-IR photodetector combining graphene and a ferroelectric crystal, namely, lithium niobate. We discuss the design, fabrication and characterization of this type of detector in detail. We also describe a model that will provide guidelines for improving the performance of the detector.

In Chapter 4, we describe the implementation of an ultra-thin ceramic 3 $\%$ mol-Yttria Stabilized Zirconia (3YSZ) as a flexible and stable substrate for mid-IR nano-optics. We describe in detail the fabrication and characterization of metal nano-structures to realize optical elements like polarizers and resonant plasmonic surfaces. We also discuss the fabrication and characterization of a transparent conducting surface using graphene on 3YSZ, emphasizing the unique mechanical flexibility of the platform.

In Chapter 5, we describe a surface comprising periodic arrays of graphene nano-holes that behave as a plasmonic crystal. In the first part of this chapter, we provide details on the various parameters that control the plasmonic behavior of these surfaces. We then describe the fabrication and characterization of these nano-hole surfaces using electron beam lithography. We then show that a large-scale fabrication technique, namely, nano-imprint lithography, can be used to fabricate such periodic graphene nano-hole arrays with high performance.

Finally, Chapter 6 provides an overall summary of the thesis and highlights future activities to continue the research work.

Chapter 2

Optoelectronics in the mid-infrared

The mid-infrared (mid-IR) (3-15 μm) region is known for a myriad of applications ranging from spectroscopic sensing to thermal imaging. However, it has been a challenging region for optoelectronics; mid-IR detectors made from narrow-bandgap materials are plagued by a low signal to noise ratio, and efficient mid-IR sources have proved difficult to realize. In this chapter, we will briefly discuss the various applications and challenges in mid-IR optoelectronics. We will also discuss some material properties and the underlying physics, in order to set the stage for the chapters that follow.

The theoretical descriptions in this chapter are brief and far from exhaustive. Throughout the text, there are numerous references to literature where more detailed descriptions can be found.

2.1 Applications in the mid-IR : Overview

In the following sections, we will briefly discuss the main applications in the mid-IR that have been addressed in this thesis, namely mid-IR photodetectors and sensing.

2.1.1 Mid-IR photodetectors

The world around us is a large source of IR radiation; all objects at room temperature emit IR radiation peaked at around 9.5 μm, following Planck´s law of black body radiation. Detecting this radiation can be useful for a wide range of applications. In particular, mid-IR photodetectors are used in applications such as thermal imaging, free space communication and spectrometers [1, 4]. Figure 2.1 shows the normalized detectivity (D^*) of some of the commonly used detectors across the IR, with the mid-IR region shown by a shaded rectangle. D^* is a figure of merit used to compare photodetectors with different modes of operation.

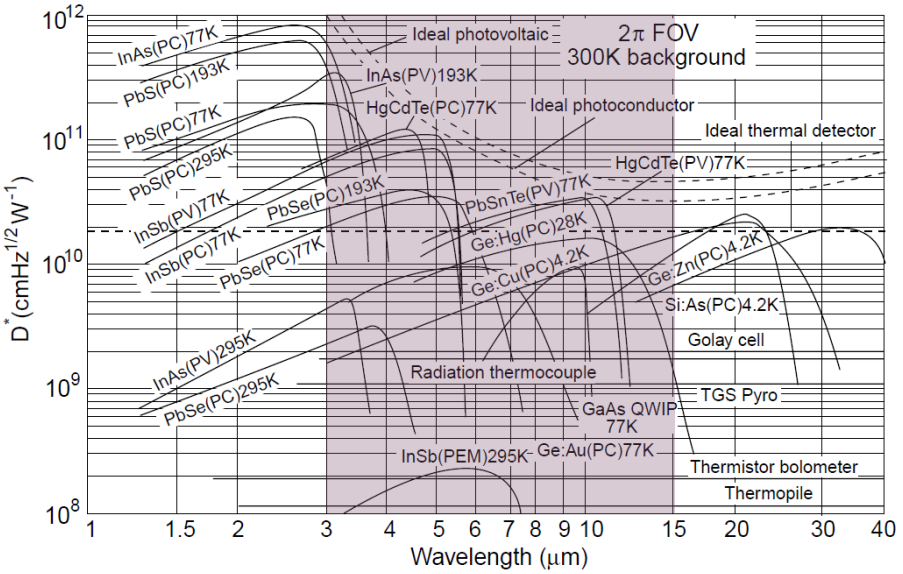

Figure 2.1: The normalized detectivity D* of various thermal and photonic detectors with their corresponding temperature of operation in the IR adapted from [1]. The mid-IR region is shown by the shaded area.

The IR photodetectors in Figure 2.1 can be broadly classified into thermal and

photon detectors, as will be described in the following sub-sections.

Thermal detectors

In thermal detectors, the absorption of incident radiation causes a change in temperature, which, in turn, causes a change in a more easily measurable property such as resistance, thermoelectric voltage, or pyroelectric voltage, which is then read in order to detect the radiation. The output signal is mostly independent of the spectral content due to the non-photonic nature of these detectors. Black coatings are generally used to enhance the absorption resulting in a broad wavelength range of operation. The three main types of thermal detectors are as follows:

i) Bolometers:

Bolometers are usually made of resistive elements (metals, semiconductors or superconductors) with a very small thermal capacity and large temperature coefficient of resistance. These resistive elements exhibit a large change in their electrical conductivity due to the heat generated by the absorption of the incident radiation. Commonly used bolometric detectors are made of vanadium oxide, amorphous silicon (a-Si), thin films of certain metals like nickel, bismuth, platinum, or antimony. Figure 2.2a shows the schematic of a typical microbolometer, arrays of which are used in thermal cameras.

ii) Pyroelectric detectors:

In pyroelectric detectors the change in temperature due to the absorption of the incident radiation results in a change in the spontaneous electrical polarization which can then be read as a change in voltage across the top and bottom surfaces. Figure 2.2b shows the schematic of a typical pyroelectric detector.

iii) Thermoelectric detectors:

Thermoelectric detectors are based on Seebeck effect i.e. the generation of a voltage difference between the junctions of two dissimilar materials due to the difference in temperature between the junctions. A thermoelectric detection element consists of two dissimilar metals connected in series. One of the junctions is blackened to absorb the radiation while the other is shielded from the radiation. The temperature rise of the irradiated junction (with respect to the non-irradiated junction) generates a thermoelectric voltage, which is then

measured to detect the radiation. Figure 2.2c shows the schematic of a typical thermoelectric detector.

The detectivities of thermal detectors are flat over the wavelength range of operation (Figure 2.1). The main advantages of these thermal detectors are that they are light, rugged, low cost and work at room temperature. However, their sensitivities are low. In addition, since heating and cooling are slow processes these detectors are slow with a response time of the order of milliseconds.

Photon detectors

In photonic detectors, the radiation is absorbed into the material by interaction with electrons either bound to lattice atoms or impurity atoms or with free electrons. The resulting change in electronic energy distribution is read as an electrical output signal, allowing the radiation to be detected. Photon detectors can be broadly divided into the following two categories depending on the types of charge carriers that are responsible for the output signal [5]:
i) Minority carrier photodetectors
Minority carrier photodetectors include photon detectors using direct band gap semiconductors and high temperature superconductors. The MCT (HgCdTe) detectors that are used in Fourier transform IR spectrometers fall into this category.
ii) Majority carrier photodetectors
Majority carrier photodetectors include photon detectors that use extrinsic semiconductors, silicon Schottky barrier devices and intersubband devices based on quantum wells.

The responses of photonic detectors exhibit wavelength dependence (Figure 2.1). They have a high signal-to-noise ratio and a very fast response, but require cryogenic cooling to prevent thermal generation of charge carriers. The need for cryogenic cooling makes them expensive and unattractive for certain applications. Nevertheless, these detectors are more widely used than thermal detectors in thermal imaging and spectrometers where high sensitivity and fast responses are required.

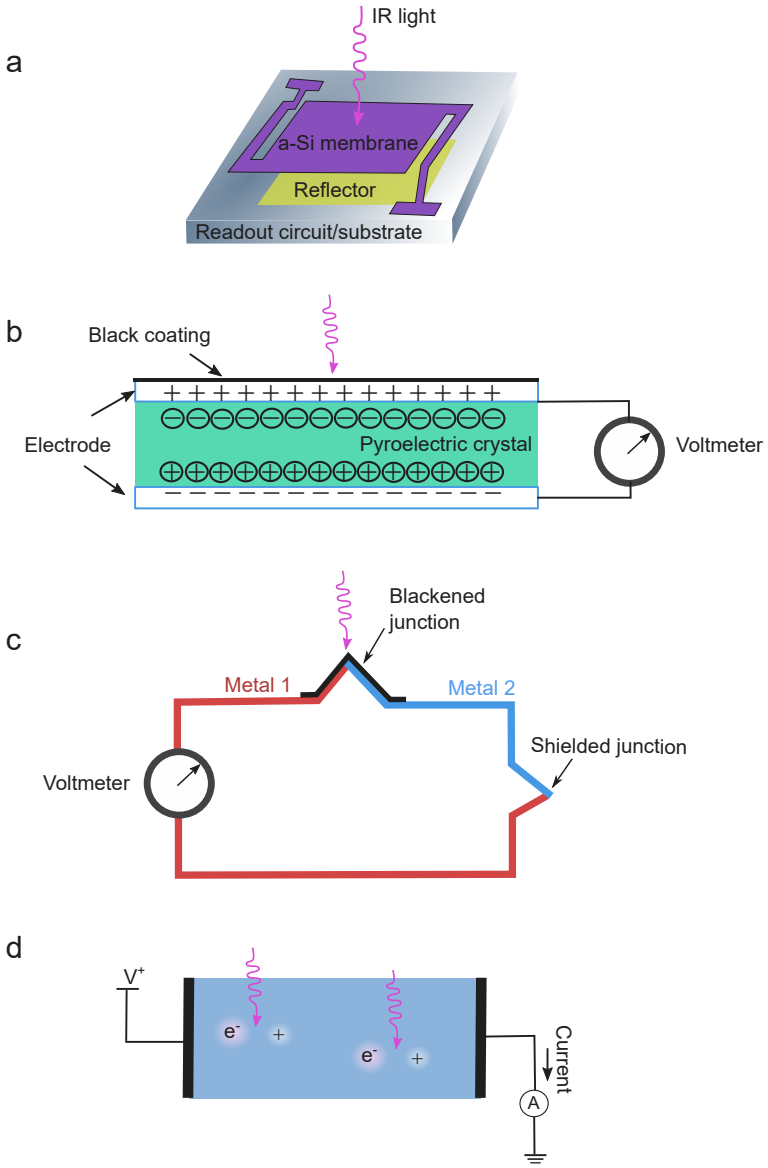

Figure 2.2: IR photodetector schemes: a) Microbolometer b) Pyroelectric detector c) Thermoelectric detector. d) Photonic detector.

2.1.2 Molecular sensing in the mid-IR

The mid-IR region is also often referred to as the 'fingerprint region' because it contains the characteristic vibrational fingerprints of many important molecules. Figure 2.3 shows the location of the vibrational fingerprints of a few such molecules [2].

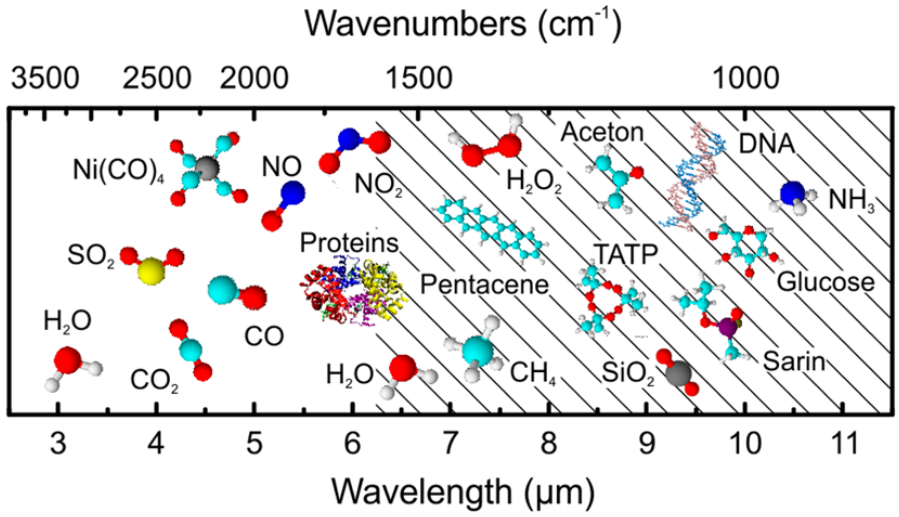

Figure 2.3: The mid-IR fingerprint region with the corresponding molecule adapted from [2].

These fingerprint vibrations contain valuable molecular information because the vibrational properties are directly related to the molecular constituents, their chemical bonds and structure. Thus spectroscopic techniques in the mid-IR are used as a label free and non-destructive method to detect and study molecules both in basic research and industry. However the size mismatch between the target molecules (few nm) and the excitation wavelength (few μm) results in low molecular absorption cross-sections $\sigma_{ab} \approx 10^{-20} cm^2$, meaning that a large amount of the target material is needed in order to observe the fingerprints. This is a challenge in applications aimed at detecting low concentrations of

molecules. However, this has been overcome to a large extent by the use of a technique called surface enhanced IR absorption (SEIRA) [6–8]. SEIRA relies on the modification of the substrate surface to enhance the local electromagnetic (EM) fields for example using surface plasmonic modes. These are described in more detail in Section 2.2.3. The first reports on SEIRA used metal particle ensembles, where sensitivities were increased by up to 3 orders of magnitude as compared to direct IR sensing.

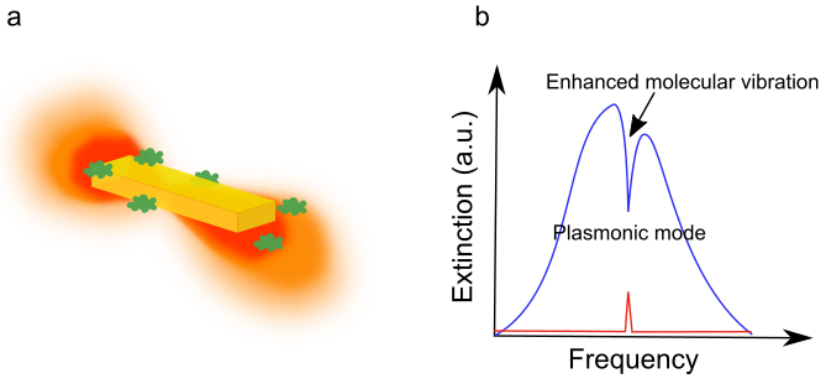

Figure 2.4: Principle of resonant SEIRA : a)Resonant metal antenna with highly enhanced local EM field. The analyte molecules are shown in green. b) Extinction of the metal antenna (blue) showing the dip corresponding to the enhanced molecular vibration of the analyte. The non-enhanced fingerprint of the analyte molecule is shown in red [2].

Later, resonant metal nanoantennas were introduced, further enhancing the sensitivity of SEIRA by upto 5 orders [7]. In this approach resonant metallic structures analogous to radio frequency (RF) antennas are designed to have their antenna resonance or plasmonic response around the vibrational resonance of the analyte molecule. Figure 2.4 shows the principle of resonant SEIRA. More details on the design of antennas for SEIRA can be found in Section 2.2.3.

2.2 Optical properties of materials

Light-matter interaction is described well by the Lorentz oscillator model where a material/medium is modelled as a collection of damped harmonic oscillators. The interaction between the light and the medium is, thus, seen as an interaction between an oscillating electromagnetic field with a collection of dipole oscillators. These dipole oscillators may originate from bound electrons, free electrons or ionic vibrations of the lattice. In insulators and semiconductors, oscillators originating from bound electrons are responsible for their optical properties at optical frequencies. Ionic vibrations in the lattice of ionic crystals are responsible for their resonances in the IR region. The optical properties of metals are dictated by free electron oscillators [9]. The following sections describe these properties, albeit briefly.

2.2.1 Dielectrics

For a dielectric material, the Lorentz oscillator model in the simplest case assumes a bound electron dipole oscillator. The global response of a medium to incident EM radiation with angular frequency ω is described by the dielectric function:

$$\epsilon_r(\omega) = 1 + \chi + \frac{Ne^2}{\epsilon_0 m_0} \frac{1}{\omega_0^2 - \omega^2 - i\omega\gamma} \tag{2.1}$$

where χ is the electric susceptibility of the medium, N is the number of atoms per unit volume, ϵ_0 is the permittivity of free space, γ is the damping and ω_0 is the resonant frequency of the electron dipole oscillator. This dielectric function/permittivity can be split into its real and imaginary part as:

$$\epsilon^{'}(\omega) = Re[\epsilon_r(\omega)] = 1 + \chi + \frac{Ne^2}{\epsilon_0 m_0} \frac{\omega_0^2 - \omega^2}{(\omega_0^2 - \omega^2)^2 + (\gamma\omega)^2} \tag{2.2}$$

$$\epsilon^{''}(\omega) = Im[\epsilon_r(\omega)] = \frac{Ne^2}{\epsilon_0 m_0} \frac{\gamma\omega}{(\omega_0^2 - \omega^2)^2 + (\gamma\omega)^2} \tag{2.3}$$

The $\epsilon^{'}$ and $\epsilon^{''}$ are related to the refractive index n and the extinction coefficient κ through the following relationship:

$$\epsilon^{'} = n^2 - \kappa^2 \tag{2.4}$$

$$\epsilon^{''} = 2n\kappa \tag{2.5}$$

A medium may have several such electronic oscillators of different resonant frequencies; in such cases the dielectric function according to the Lorentz model can be written as:

$$\epsilon_r(\omega) = 1 + \frac{Ne^2}{\epsilon_0 m_0} \sum_j \frac{1}{\omega_j^2 - \omega^2 - i\omega\gamma_j} \tag{2.6}$$

This takes into account all transitions in the medium and hence enables us to estimate the full frequency dependence of the dielectric constant of the material. Figure 2.5 shows the dielectric function of a dielectric, namely lithium niobate, that is used in Chapter 3 as a substrate [10].

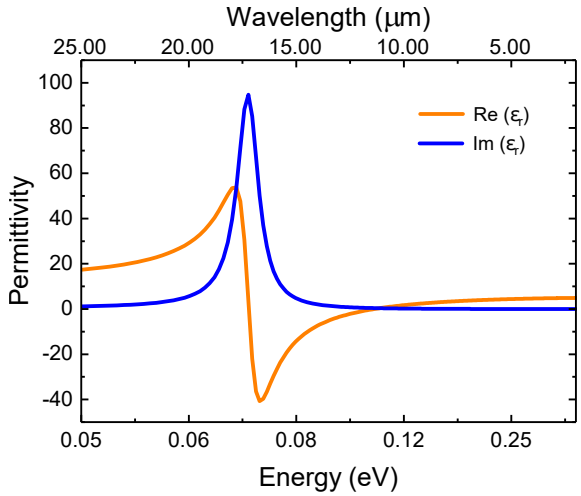

Figure 2.5: Permittivity of lithium niobate, calculated using the Lorentz oscillator model. The real part of the permittivity is shown in orange and the imaginary part in blue.

2.2.2 Metals

A metallic medium can be described as a plasma consisting of a stationary ionic core and free electrons. The permitivity of a metal can be described by combining the features of the free electron model proposed by Drude and the Lorentz dipole model described previously. The Drude-Lorentz model for metals is obtained by assuming that no restoring force exist for the Lorentz oscillators described in Section 2.2.1. The dielectric function is then given by:

$$\epsilon_r(\omega) = 1 - \frac{Ne^2}{\epsilon_0 m_0} \frac{1}{\omega^2 + i\omega\gamma_{met}} = 1 - \frac{\omega_p^2}{\omega^2 + i\omega\gamma_{met}} \tag{2.7}$$

where γ_{met} is the damping and $\omega_p = Ne^2/\epsilon_0 m_0$ is the characteristic plasma frequency of the metal. Figure 2.6 shows the dielectric function of gold in the IR.

The optical properties of a metallic medium can also be described by its AC conductivity which is related to the ϵ_r by the relation:

$$\epsilon_r(\omega) = 1 + \frac{i\sigma(\omega)}{\epsilon_0 \omega} \tag{2.8}$$

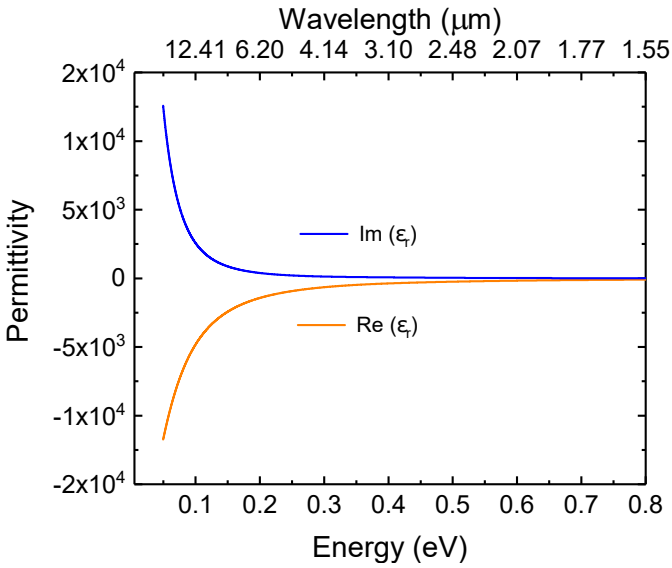

Figure 2.6: Permittivity of gold in the IR calculated using the Drude-Lorentz model with ω_p=$1.38 \times 10^{16}\ rad/s$, $\gamma_{met} = 3.66 \times 10^{14}\ rad/s$.

2.2.3 Plasmonics

As mentioned previously, plasmonic structures have been widely used to focus radiation down to sub-wavelength volumes and aid in improving the sensitivity in SEIRA. In the following sections, we will describe the basic concepts outlining plasmonics.

Plasmons are collective oscillations of free electrons in a conductor. They can be thought of as mechanical oscillations of the electron gas with respect to the stationary ionic cores, in the presence of an external electric field. For bulk or volume plasmons, these oscillations occur at the volume plasma frequency ω_p defined in Equation 2.7 [11, 12].

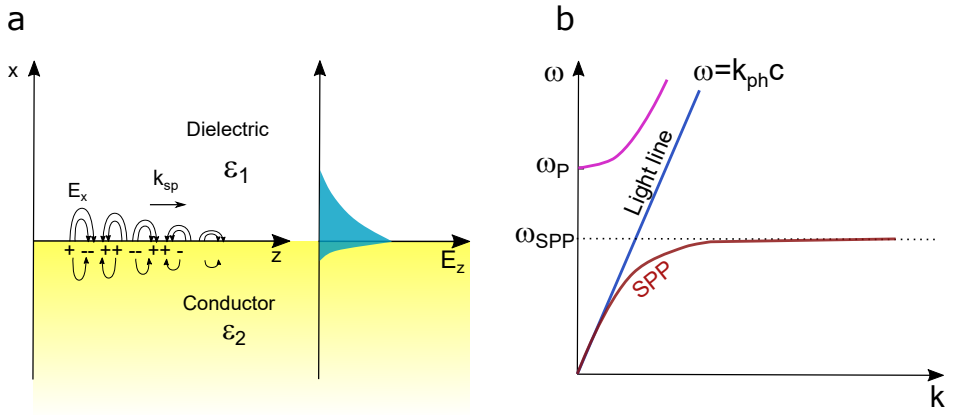

Figure 2.7: a) Illustration of surface plasmon polaritons at the interface of a conductor (yellow region) and dielectric (white region). The evanescent electric field (blue) of the surface plasmon polariton is shown on the right. b) The dispersion curve of the SPP (red) at the interface between a conductor and a dielectric. The dispersion of the bulk plasmons is shown in pink.

At the interface between a conductor and a dielectric media, plasmons can take the form of surface plasmon polaritons (SPPs), often referred to as surface plasmons (SPs). Surface plasmon polaritons are electromagnetic excitations propagating at the interface between a dielectric and a conductor, evanescently confined in the perpendicular direction. These electromagnetic surface waves result from the coupling of the electromagnetic fields of an incident radiation to oscillations of the conductor's electron plasma. The dispersion relation of these SPs is given by:

$$k_{sp} = k_{ph}\sqrt{\frac{\epsilon_1\epsilon_2}{\epsilon_1+\epsilon_2}} \tag{2.9}$$

where k_{ph} is the wave vector of the incident, ϵ_1 is the permittivity of the dielectric and ϵ_2 is the frequency dependent dielectric function of the conductor given by the Drude model (Equation 2.7).

A prerequisite for such transverse magnetic(TM) SPP modes to exist is that $\epsilon_1\epsilon_2 < 0$ [12]. Due to their high confinement and sensitivity to the surrounding

dielectric media, they are widely exploited in many applications such as enhanced sensing and energy collection for detectors and sub-diffraction limited waveguiding.

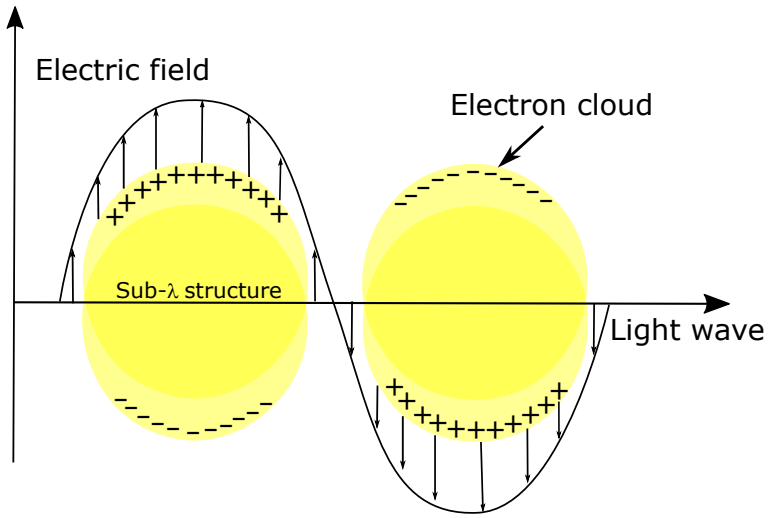

Figure 2.8: Illustration of a surface plasmon confined in a sub-wavelength structure.

When a surface plasmon is confined to a structure of dimensions comparable to the wavelength of the incident light,it is termed a localized surface plasmon (LSP). As a result,the electric fields near the surface of these sub-wavelength structures are greatly enhanced (Figure 2.8) his enhancement is highest at the surface and rapidly decreases with distance. The optical extinction of such a structure has a maximum at the plasmon resonant frequency, which occurs at visible wavelengths for noble metal nanostructures. For longer wavelengths like the mid-IR , metals have low confinement and hence do not provide the real advantage of using plasmonic structures. Even so, metal dipole antenna arrays have been used to couple incident mid-IR radiation to absorbing molecules. These antennas are sometimes referred to as plasmonic, the resonant wavelength

of an isolated antenna at mid-IR wavelengths scales almost linearly with antenna length, a result of the quasi-perfect electrical conductor nature of noble metals in this wavelength range [13–15]. Thus, the observed resonances are closer to those of a traditional antenna than the localized plasmonic resonances utilized at the visible and near-IR wavelengths. However, graphene with its tunable plasma frequency in the mid-IR provides an ideal platform for plasmonics with high confinement in the mid-IR, as will be described in the following section.

2.3 Graphene for mid-IR optoelectronics

Graphene, the 2D allotrope of carbon, has gained a remarkable amount of attention from the scientific community since its discovery and isolation in 2004 [16, 17]. Graphene has been used in many optoelectronic applications such as photodetection, transparent conduction and sensing. In this section, we will discuss the optoelectronic properties of graphene that are relevant for applications in the mid-IR.

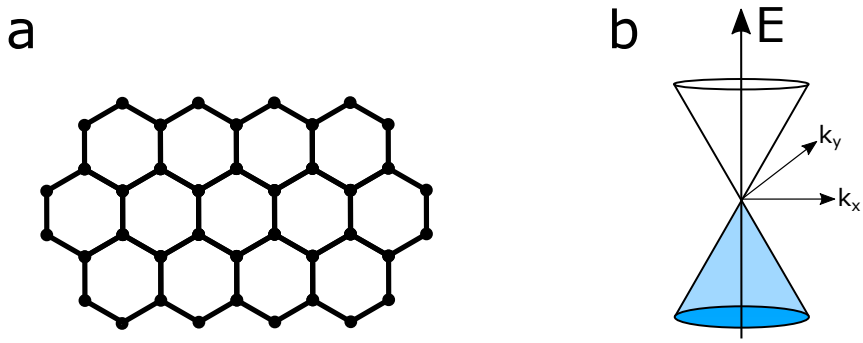

Figure 2.9: a) Carbon atoms (represented by disks) arranged in the hexagonal honeycomb lattice. b) The linear energy-momentum dispersion of graphene where the conduction and valence bands meet at the Dirac point. The valence band is filled up to the Dirac point (shown in blue) and $E_F = 0\ eV$

Graphene is a monoatomic layer of sp^2 hybridized carbon atoms positioned in a hexagonal honeycomb lattice. Such an arrangement of atoms gives rise to

the peculiar band structure of graphene where the valence band and conduction band touch each other at a point which is often referred to as the Dirac point or the charge neutrality point (CNP). Hence, graphene is often referred to as a zero-band gap semiconductor or a zero-overlap semimetal.

For energies of less than $1eV$ the energy-momentum dispersion is linear and hence charge carriers in graphene are characterized by zero effective mass. Thus the carrier dynamics is described by the relativistic Dirac equation rather than the non-relativistic Schrodinger equation with an effective mass [18, 19]. The charge carriers in graphene have a relativsitic Fermi velocity of $v_F = c/300$, where c is the speed of light in vacuum. The Fermi energy in graphene can be tuned by changing the carrier density:

$$E_F = \hbar v_F k_F = \hbar v_F \sqrt{\pi n_s} \tag{2.10}$$

where $\hbar$ is the reduced Planck constant and k_F is the Fermi wave vector. The unique band structure of graphene is responsible for the many extraordinary properties exhibited by it. In the next section, we will discuss the electrostatic tunability of the electronic properties of graphene.

2.3.1 Tunable properties of graphene

Due to its two dimensional nature and zero band gap, free carriers can be easily induced in graphene by electrostatic (electric field effect) or chemical means. Figure 2.10 shows a typical graphene field effect transistor (FET) in a back-gated configuration. A back-gate voltage V_{BG} is applied between a layer of highly conductive silicon (Si^{++}) and the graphene, with a thin dielectric of silicon dioxide (SiO_2) in between them. Such a configuration, resembles a capacitor with the back-gate Si^{++} and the graphene acting as the two plates of the capacitor. Thus, charges accumulate on the graphene as a function of the applied V_{BG}. Therefore, the n_s can be calculated using a simple capacitor model:

$$n_s = \sqrt{((V_{BG} - V_o)C_{ox}/e)^2 + n_o^2} \tag{2.11}$$

where V_0 is the backgate voltage at which the CNP appears, n_0 is the intrinsic carrier density which depends on the graphene quality and the mobility and C_{ox}

is the capacitance of the oxide given by: $C_{ox} = \epsilon_o \epsilon_{ox}/t_{ox}$ where ϵ_o is the permittivity of free space, ϵ_{ox} is the perimittivity of the SiO_2, t_{ox} is the thickness of the SiO_2 layer.

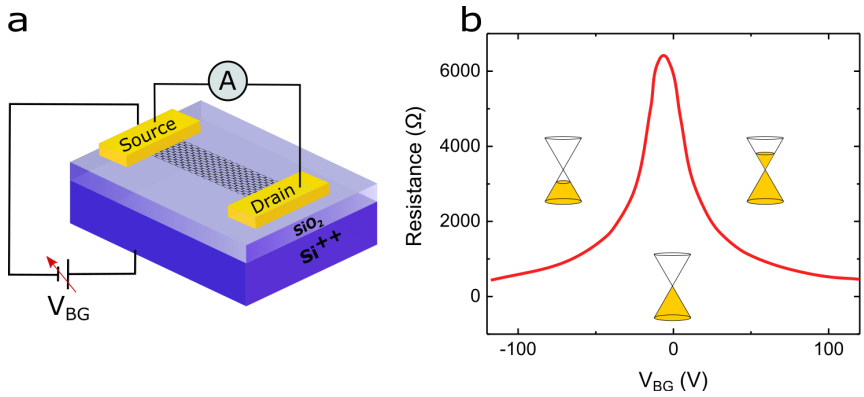

Figure 2.10: a) A typical two-probe graphene device (Graphene FET) that can be electrostatically tuned.b) Ambipolar field effect in graphene. The inset shows the position of the Fermi level in the Dirac cones. Filled regions are indicated by the colored regions.

This change in n_s as a function of V_{BG} translates to a change in the resistance of the graphene device (as shown in Figure 2.10b) and can be measured across the source and drain contacts. The resistance is the highest yet finite at the CNP due to the absence of a band gap. The inset of Figure 2.10b shows the shift in the Fermi level (E_F) as the doping type transitions from n-type (positive V_{BG}) to p-type (negative V_{BG}) doping through the CNP. The conductivity of graphene is related to the n_s by the relation $\sigma = n_s e \mu$ where μ is the mobility of the graphene. Although the band structure of graphene supports the relativistic transport of charge carriers, in reality the mobility is limited by several factors. For instance interaction with substrate phonons, charged impurities and lattice defects can all cause a significant reduction in the mobility.

2.3.2 Optical properties of graphene

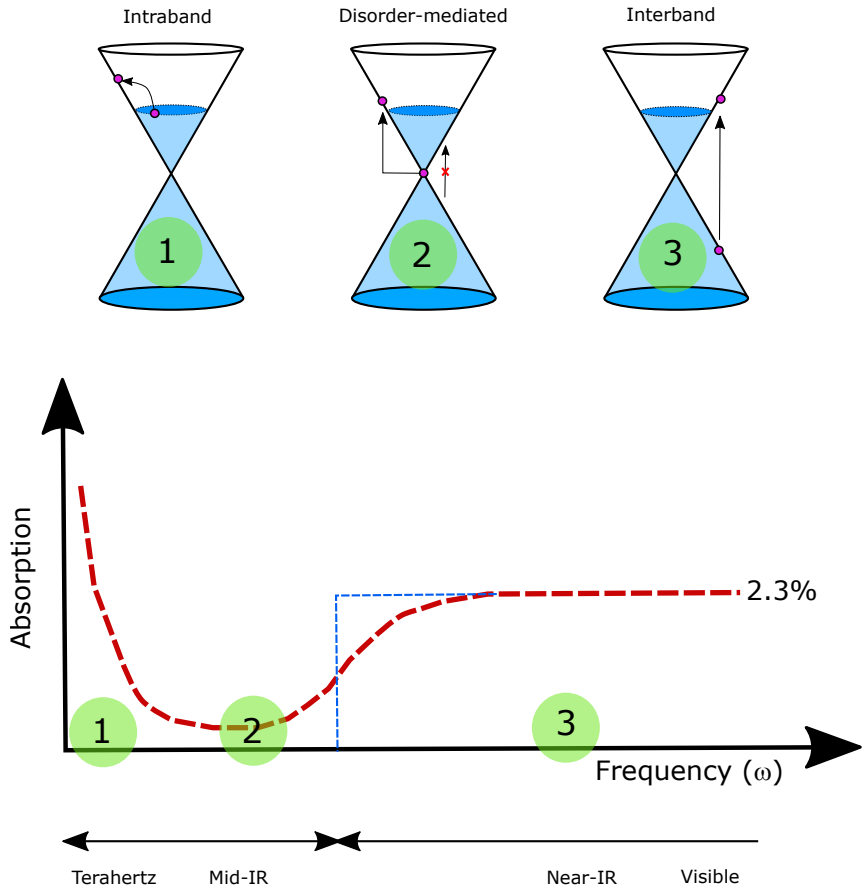

Figure 2.11: Illustration of the typical absorption regimes in doped graphene. The characteristic features of the absorption spectrum like the universal absorption at visible and near-IR, minimal absorption in mid-IR and Drude peak at terahertz frequencies, are shown.

Graphene absorbs in a broad range of frequencies because of its zero-band gap.Intrinsic graphene is characterized by its universal optical conductivity $e^2/4\hbar$

where e is the electronic charge and $\hbar$ is the reduced Planck´s constant. This gives rise to the well-known universal absorption of 2.3 $\%$ in the region from visible to near-IR frequencies [20]. This value of universal absorption is true only for suspended graphene. At frequencies where E_{ph} $>2E_F$ (visible and near-IR) the absorption is due to direct interband transitions. At frequencies where E_{ph} $<2E_F$, the direct interband transition is prohibited by Pauli´s exclusion. However, experiments show that disorder mediated absorption occurs at these frequencies. Hence the absorption at these frequencies is non-zero but less than the universal absorption of graphene. The non -zero absorption at mid-IR frequencies is attributed to such disorder mediated transitions. At frequencies where $E_{ph} \ll 2E_F$,for example in the tera-hertz region, the absorption is mainly due to intraband transitions and is characterized by increased absorption (Drude peak) [21].

The mathematical description of the optical properties is given by the optical conductivity; which for the mid-IR range where intraband processes dominate is given by the Kubo formula as [22–24]:

$$\sigma_{intra}(\omega) = \frac{\sigma_0}{\pi}\frac{4}{\hbar\gamma - i\hbar\omega}[E_F + 2k_BTln(1 + e^{(-E_F/k_BT)}] \tag{2.12}$$

where ω is the angular frequency of the excitation light, γ is the carrier scattering rate in graphene, $\hbar$ is the reduced Planck constant and σ_0 is the universal optical conductivity of graphene. Since E_F can be tuned electrostatically and by chemical doping, the optical conductivity of graphene is tunable. The optical conductivity of graphene calculated using the Kubo formula is shown in Figure 2.12 This formula has been used in all the calculations done in the thesis.

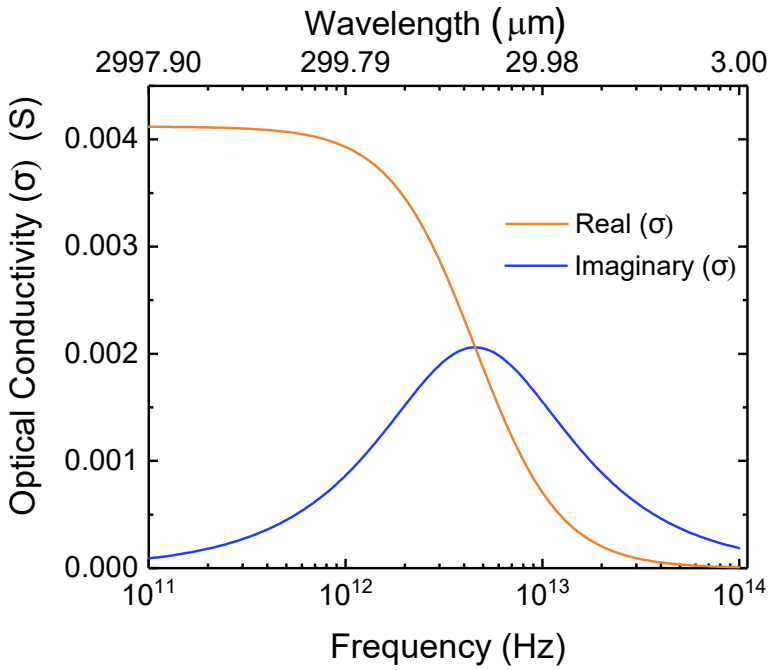

Figure 2.12: The real (orange) and imaginary (blue) parts of the optical conductivity of graphene calculated using the Kubo formula considering only intraband processes with $1/\gamma = 35\ ps$ and $E_F = 1\ eV$.

2.4 Plasmons in graphene

The SP modes discussed in Section 2.2.3 can also be excited in graphene, giving rise to highly confined plasmonic modes.Figure 2.13 shows a simple dielectric–graphene–dielectric system that accommodates a TM plasmon mode. [25, 26]. For a detailed description one can refer to Jablan *et al.* [25].

The plasmon wave vector k_{gsp} can be described by the following equation:

$$k_{gsp} = \frac{i2\omega\epsilon_{d12}\epsilon_0}{\sigma(\omega)} \tag{2.13}$$

where $\epsilon_{d12} = (\epsilon_{d1}+\epsilon_{d2})/2$ is the average permitivitty of the surrounding medium

and $\sigma(\omega)$ is the frequency dependent conductivity of graphene.

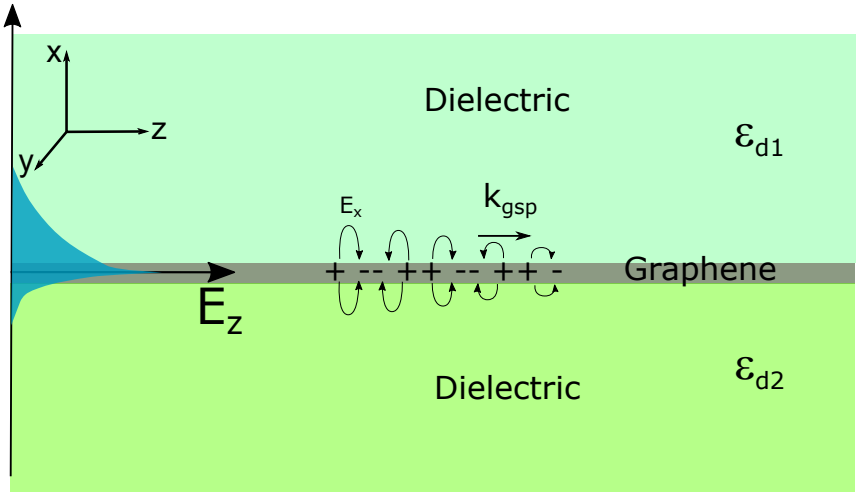

Figure 2.13: Illustration of a TM plasmon mode in graphene (grey) placed between two dielectrics with dielectric constants ϵ_{d1} and ϵ_{d2}. The highly confined electric field distribution is shown in blue.

As discussed in sub-section 2.3.2, at long-wavelengths (mid-IR or Terahertz) the optical conductivity is dominated by intra-band transitions. Thus the plasmon dispersion in Equation 2.13 can be written as:

$$k_{gsp}(\omega) = \frac{2\pi\hbar^2\epsilon_0\epsilon_{d12}}{e^2E_F}\omega^2(1+\frac{i}{\tau\omega}) = \frac{\epsilon_{d12}}{2\alpha}\frac{\omega}{\omega_F}k_{ph}(1+\frac{i}{\tau\omega}) \tag{2.14}$$

where $\alpha = e^2/4\pi\hbar\epsilon_o c$ is the fine structure constant and $\omega_F = E_F/\hbar$.

Assuming that the imaginary part of the conductivity (i.e the absorption)=0 , we can obtain the plasmon dispersion relation, which depends on $\sqrt{k_{gsp}}$ as:

$$\omega_{pl} = \sqrt{\frac{e^2E_Fk_{gsp}}{2\pi\hbar^2\epsilon_o\epsilon_{d12}}} \tag{2.15}$$

Thus from Equation 2.15 one can estimate that with the doping levels achievable by electrostatic doping ($E_F = 0.2 - 0.4\ eV$), the plasmon frequency of the system will lie in the mid-IR.

In the mid-IR, for typical values of Fermi energy, $\omega/\omega_F \approx 1$, so confinements of the order $1/\alpha \approx 1/137$ can be achieved. This means that electromagnetic energy is confined to a volume $\approx 10^6$ times smaller than in the free space. Such a small confinement, of electromagnetic energy has applications in many areas of nanophotonics. The in-situ tunability of the plasmon frequency by changing the n_s makes it a unique platform for such applications.

Due to the large wave vector (momentum) mismatch between the incident light and the plasmon, plasmons cannot be excited in homogeneous graphene sheets. Instead, engineered graphene structures like ribbons, disks etc. have been used in literature to excite plasmon resonances in the Terahertz and mid-IR. [27, 28].

As described in the different chapters of this thesis, we have exploited several of the above mentioned material properties to implement optoelectronic components for mid-IR.

Chapter 3

Graphene on ferroelectrics for infrared photodetection

3.1 Introduction

There is great interest in developing photodetectors for infrared (IR) wavelengths, as they are essential components in many applications, e.g. vibrational spectroscopy and thermal imaging [1]. State-of-the-art IR-photodetectors (e.g. HgCdTe based) can reach high detectivities ($<10^{10}$ cm$\sqrt{Hz}$/W) but they usually operate at very low temperatures in order to achieve sufficiently low noise levels. This is because these are photon detectors in which electrons are excited directly by the absorption of radiation and hence cooling to liquid nitrogen temperature (77K) is necessary to avoid interefering excitation of electrons by thermal motion. One class of IR-photodetectors that avoid cryogenic cooling is based on pyroelectricity. Pyroelectricity is the ability of certain crystals or poly crystalline materials to develop a change in the magnitude of electric polarization in response to a change in temperature. Only 10 of the 32 classes of crystal structures exhibit pyroelectricity [29]. These materials have a spontaneous polarization (bound charges) even in the absence of an electric field. The relationship between the change in surface charge density and the change

in temperature is given by:

$$\sigma_{pyro} = \gamma_{pyro}(T)\Delta T \tag{3.1}$$

where $\gamma_{pyro}(T)$ is called the pyroelectric coefficient and is a characteristic of the material and ΔT is the change in temperature.

In a sub-group of pyroelectric materials, called ferroelectric materials, the spontaneous polarization can be reversed by the application of an electric field. These materials have higher pyroelectric coefficients than the non-ferroelectric pyroelectrics. In these ferroelectrics, pyroelectricity is observed only below a certain temperature called the Curie temperature (T_c). Examples of such materials include lithium niobate ($LiNbO_3$), lithium tantalate ($LiTaO_3$) and triglycine sulfate (TGS). Majority of these crystals have a T_c of several hundreds of kelvins.

When IR radiation is absorbed by the pyroelectric substrate and converted into heat, a temperature variation is produced. This in turn induces surface charges which can be measured by voltage difference across the substrate surfaces or by current through an external shunt resistor. The performance of pyroelectric based photodetectors strongly depends on the dielectric constant (ϵ_r) and loss (tan δ) of the substrate material [30, 31]. The lower the ϵ_r and tan δ, the higher the sensitivity. Unfortunately, materials with a high pyroelectric coefficient typically have a high ϵ_r and/or tan δ which poses severe limitations to the photodetector sensitivity.

As discussed in the previous chapter, because of its electrical transport and optical properties, graphene and other 2-D materials have been investigated as promising candidates for IR photodetection [32–36]. Graphene is known to interact strongly with the substrate and to have its electronic properties influenced by its environment. This is evident from changes in its mobility and intrinsic doping from substrate to substrate [37, 38]. In this work, we have exploited the strong interaction between graphene and a ferroelectric substrate to implement a photodetector working in the IR [28, 39–41].

In one of the first attempts, Hsieh *et al.* reported an opto-thermal field effect transistor (FET) using graphene on a lead zirconate titanate (PZT) substrate, where the drain current was modulated using a near-IR laser (1064 nm), with an amplitude of 3. 6×10^{-4}A/W [42]. The achieved quasi-Direct current (DC)

modulation of the current through light absorption was measured with mm-sized graphene devices and was related to changes in the graphene resistance through pyroelectric charges on the PZT surface. Although revealing the opto-thermal effect, the frequency response and a full description of the mechanism to be used in photodetectors were not addressed.

More recently, an IR-photodetector based on graphene on polyvinylidene fluoride (PVDF) substrate was reported by Kulkarni *et al.* [43]. In this case, graphene was used as a transparent electrode in a classical pyroelectric detector configuration, exploiting its transparency in the IR region.

Baeumer *et al.* instead reported spatial carrier density modulation in graphene on periodically poled $LiNbO_3$ [44]. Taking advantage of the fact that charges of different signs are induced in oppositely oriented domains, they were able to demonstrate a p-n junction photodetector by applying a gate voltage across the domain inverted structure, with a responsivity of $2 \times 10^{-5} A/W$ in the visible range.

As will be described in the following sections, we combined $LiNbO_3$ and graphene to implement a photodetector working in the IR. As a starting point, we will describe the properties of lithium niobate relevant to our detector.

Lithium niobate

$LiNbO_3$ is an ABX_3 type crystal that is chemically stable and ferroelectric below 1415 K. Above the Curie temperature the chemical structure of ferroelectric $LiNbO_3$ consists of planar sheets of LiO_3 and Nb atoms piled along the c-axis.In this temperature range, $LiNbO_3$ is non polar as the nominal valence states add to zero. But below the Curie temperature, the elastic forces of the crystal are dominant and hence Nb and Li ions leave their positions. The resulting charge separation makes the crystal polar with a high spontaneous surface charge density along the c axis.

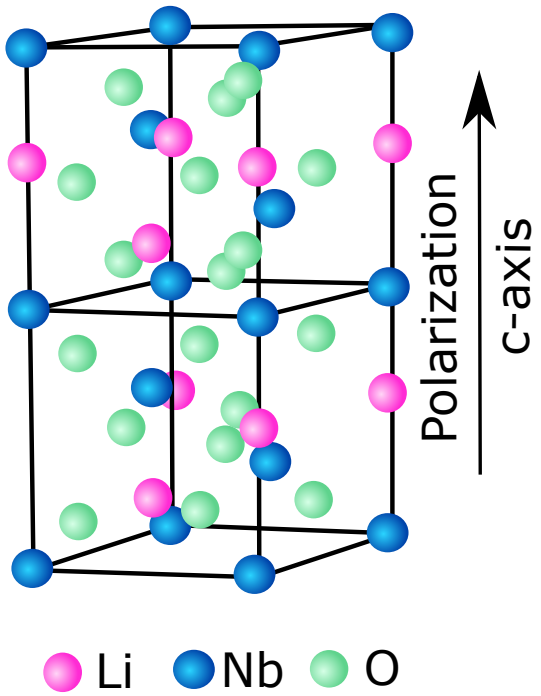

Figure 3.1: The ABX_3 crystal structure of ferroelectric $LiNbO_3$. The Li, Nb and O atoms are represented by circles of pink , blue and green respectively.

Cutting the crystal perpendicular (Z-cut) to this axis results in a crystal that has different signs of spontaneous surface charge density on the top and bottom surfaces (Figure 3.1) [45, 46].

$LiNbO_3$ exhibits high absorption in the 6 to 10 μm wavelength range, which is attributed to multi-phonon absorption (Figure 3.2). In our experiments, we use Z-cut $LiNbO_3$, which has a pyroelectric coefficient of -83 $\mu C/K/m^2$ at 300K.The negative sign indicates that an increase in temperature causes a decrease in the surface charge density of the $LiNbO_3$ and vice versa.

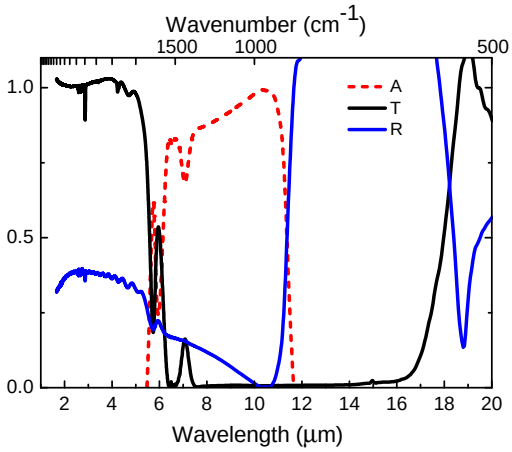

Figure 3.2: Transmission (black) and Reflection (blue) spectra of 500 μm thick Z-cut $LiNbO_3$. The absorption is shown by the dotted lines in red.

The photodetector reported by us exploits the high absorption and pyroelectric coefficient of $LiNbO_3$ and the high doping sensitivity of graphene, as will be described in detail in the following sections.

3.2 Pyroelectrical doping of graphene

3.2.1 Devices

The devices were fabricated on the +Z face of 500 μm thick $LiNbO_3$ substrates (MTI Corporation).The substrates were cleaned using organic solvents followed by a diluted basic piranha solution to remove any impurities that might prevent good adhesion between the graphene and the substrate. To avoid thermal shock and to aid the discharge of static charges (due to the pyroelectric nature of the substrate),all baking processes were carried out with a slow ramp of temperature. Ultraviolet (UV) lithography was used to define 2-probe and 4-probe (Hall geometry) devices on the substrate. Subsequently, Chromium (Cr)

(5 nm)/Gold (Au) (100 nm) contacts were deposited by thermal evaporation and lifted off using acetone. Additionally, the rear sides of all substrates were coated with Cr (5 nm)/Au (100 nm) to aid the discharge of the static charges and act as a thermal sink.

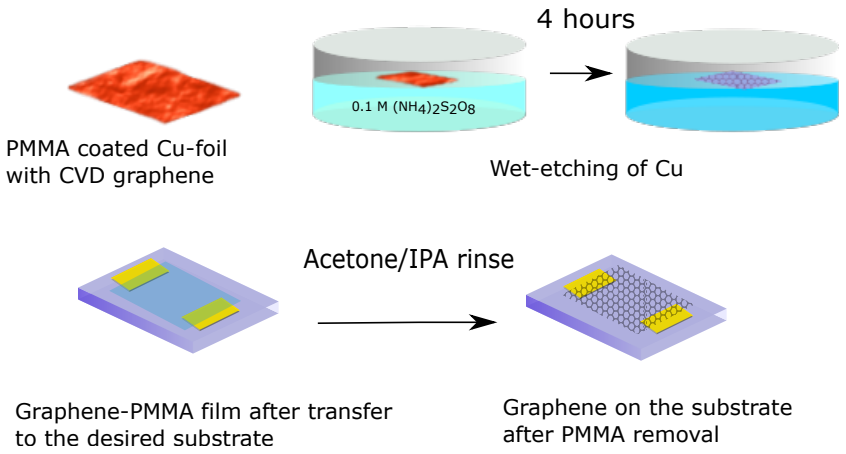

Figure 3.3: Schematic showing the transfer of CVD graphene on a substrate by the wet-etching method.

All the graphene devices described in this thesis, including the ones on $LiNbO_3$, use chemical vapor deposition (CVD)-derived graphene. Figure 3.3 shows the schematic of the wet-transfer technique used to transfer CVD graphene onto a substrate [47]. The CVD graphene on copper (Cu) foil was either made at ICFO or bought from Graphenea, and the transfer of the CVD graphene was carried out by wet etching of the Cu foil beneath the graphene. The Cu-foil was coated with a poly-methyl methacrylate (PMMA) layer as a supporting layer for the wet-etching. The Cu/graphene/PMMA film was then allowed to float on a 0.1M filtered solution of Ammonium persulfate for 4 hours in order to achieve a complete etching of the Cu foil, and the resulting free-standing PMMA/graphene membrane was immersed in water for 10 minutes to remove any remnants of the etchant. After that, the PMMA/graphene membrane was

placed on the desired target substrate and left to dry in a desiccator for 24 hours. Subsequently, the PMMA on top of the graphene was dissolved with acetone and then rinsed with isopropyl alcohol (IPA), resulting in a graphene film on the desired substrate. In order to define the device geometries, UV optical lithography and subsequent reactive ion etching (RIE) using argon (Ar)/oxygen (O_2) radio frequency plasma at 10 W for about 1 minute.

3.2.2 Temperature gating of graphene

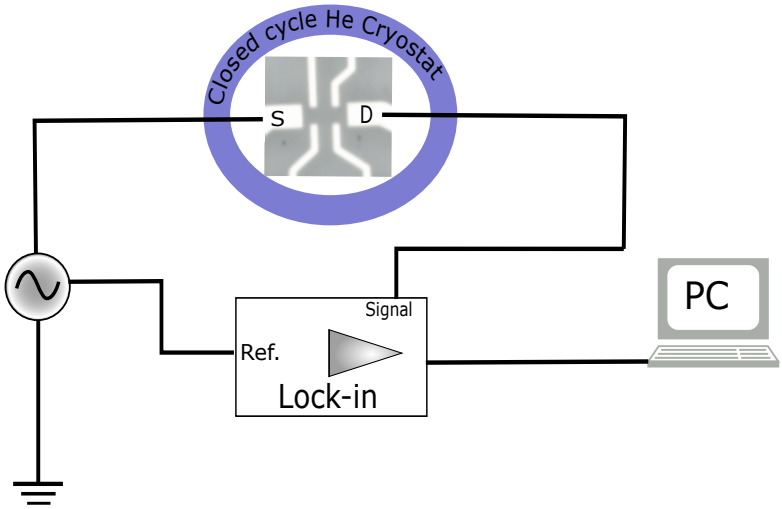

Figure 3.4: Schematic of the experimental set up for temperature gating of graphene on $LiNbO_3$. The S and D are the source and drain contacts of the 4-point probe device.

In order to study the pyroelectrically induced doping, the sheet resistance of graphene deposited on $LiNbO_3$ was measured upon temperature variation.

Measurements were taken using a 4-probe configuration in a Hall bar geometry while sweeping the temperature of the chip across a few tens of °C in vacuum (P$\leq 10^{-5}$ mbar) in a closed cycle helium cryostat. The resistance of the devices was monitored by using a lock-in amplifier and measuring the voltage drop across the graphene Hall bar, while injecting a 1 μA alternate-current (AC) at 503 Hz (Figure 3.4). Any change in temperature of the device leads to a subsequent change in the spontaneous polarization of the $LiNbO_3$ due to the pyroelectric effect. Since the pyroelectric coefficient of $LiNbO_3$ is negative there is a decrease in the $LiNbO_3$ bound (polarization) surface charge density which then induce (capacitively) free charges into the graphene.

As shown in Figure 3.5, temperature variations induce a change in resistance moving across the charge neutrality point (CNP) and the typical Lorentzian shape associated with the field effect (described in Chapter 2) can be observed. We have converted the variation of temperature with respect to the charge neutrality point (ΔT) into the carrier density induced in the graphene (n),in contact with $LiNbO_3$. The conversion is readily obtained via the relation:

$$n = \frac{\gamma_{pyro}(T)}{e}\Delta T \tag{3.2}$$

where e is the electron charge and ΔT is the change in temperature as defined in Equation (3.1).

The fitting of the curve was performed with the Lorentzian model for the resistivity of graphene as a function of the carrier density:

$$R(n) = R_c + N_{EQ}\frac{1}{e\mu\sqrt{n_0^2 + n^2}} \tag{3.3}$$

where R_c is the contact resistance of the device, N_{EQ} is the number of equivalents of sheet resistance (R_s) of the device and depends on the geometry and patterning of graphene (for the device used for Figure 3.5 $N_{EQ} = 1.25$),μ is the mobility and n_0 is the doping related to the intrinsic impurities in graphene. The parameters for the curve fitted in Figure 3.5 are: R_c=440Ω, μ=4639 cm^2/Vs, $n_0 = 3.5 \times 10^{11} cm^{-2}$.

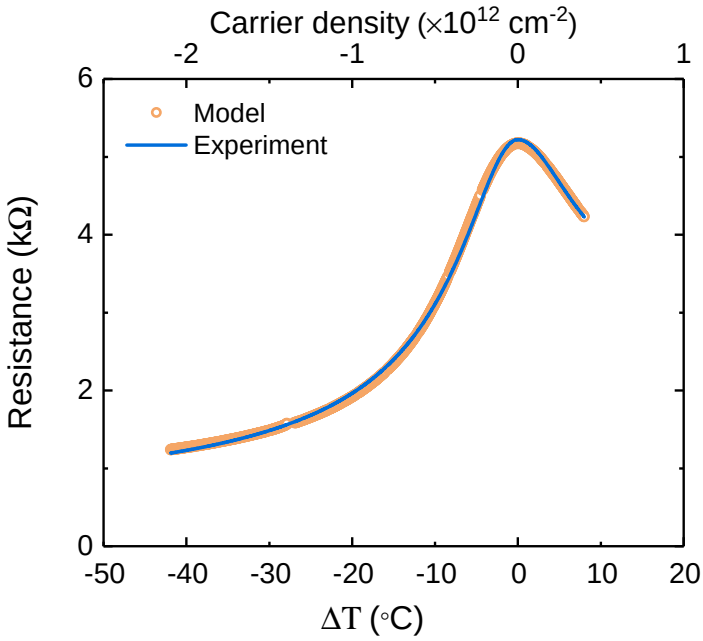

Figure 3.5: Pyroelectrically induced doping and resistance change in graphene on $LiNbO_3$ during cooling (heating) in a closed cycle helium cryostat. The curve sweeps across the charge neutrality point (CNP) without the need of an external gate voltage

3.3 Photodetection using pyroelectric doping of graphene

The basic principle of photodetection using pyroelectric doping is shown in Figure 3.6. The impinging light is absorbed by the substrate and subsequently converted into heat, resulting in a local temperature increase. This produces a variation in the spontaneous polarization of the $LiNbO_3$ due to the pyroelectric effect. Since the pyroelectric coefficient of $LiNbO_3$ is negative, there is a decrease in the $LiNbO_3$ bound (polarization) surface charges which then induces (capacitively) free charges into the graphene [48].

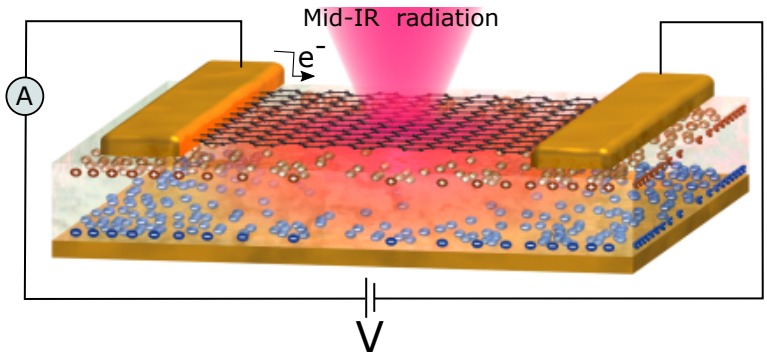

Figure 3.6: Photoresponse mechanism used in the graphene on $LiNbO_3$ photodetector

Through this process, the light induces a change in the electrical resistance (conductance) of the graphene channel. This phenomenon is called the pyroresistive effect and can be exploited to obtain a new generation of photodetectors. Indeed, the characteristics of such detectors lie between those of pyroelectric ones and bolometers as they use the pyroelectricity of the substrate to induce doping (as with pyroelectric detectors) and the read-out is based on the resistance change in the graphene (as with bolometers). The proposed approach can potentially lead to an optimum trade-off between both types of detectors, overcoming their intrinsic limitations when taken individually.

3.3.1 Photoresponse measurement

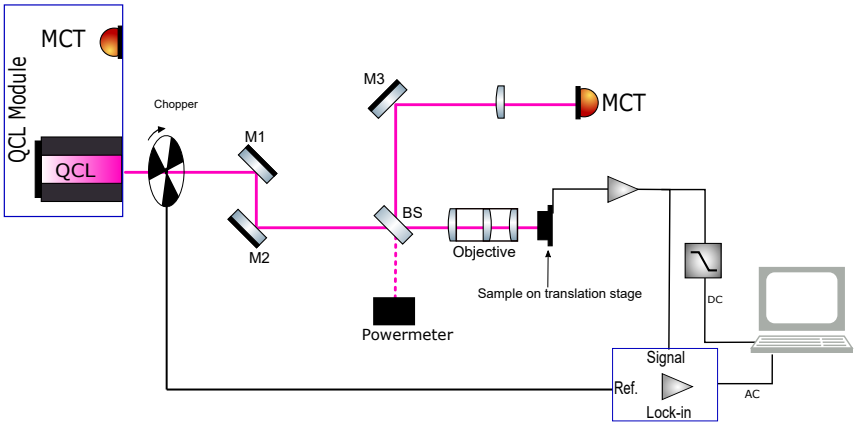

Figure 3.7: Schematic of the experimental set up used for photoresponse measurement.

To study this conversion of optical signals into a variation of the graphene channel resistance, i.e. a pyro-resistive photodetector,we measured the photoresponse of several devices, that had a two-point probe geometry. The photoresponse measurements, which included spatial mapping, were taken by illuminating the device with a tightly focused light beam from a quantum cascade laser (QCL) operating in the 1000-1600 cm^{-1} range. The sample was mounted on a motorized stage and moved across the focussed beam from a laser. The full-width half maximum (FWHM) of the spot size was comparable to the wavelength. The laser light was modulated between 1-1000 Hz using an optical chopper. A source-drain DC voltage of 0.1 V was applied to the graphene devices across the metallic side contacts.The photocurrent was amplified using a Femto DLPCA-200 preamplifier and the lock-in signal was obtained with a Stanford Research Systems SR830 DSP. For the DC photocurrent map measurements were carried out with continuous (unchopped) light and using a 1 Hz low-pass filter after the current amplification. This configuration permitted

the resolution of the photoresponsivity not only spatially, but also with respect to the excitation frequency.

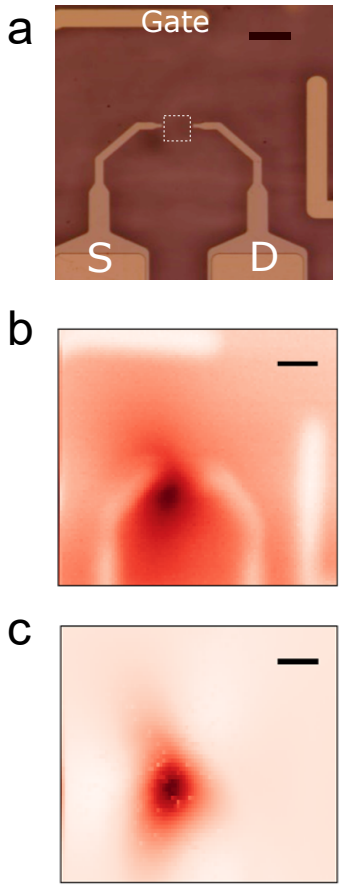

Figure 3.8: a) Two probe device used for photoresponse measurements. The area of the graphene is shown by the white square. b) Normalized photoconductivity map in DC. c) Normalized photoconductivity map in AC (77 Hz). Scale bars are 100 μm.

The normalized photoresponse is the ratio of the photocurrent observed when the laser is focussed at a point to the maximum value of photocurrent observed on the device. This photoresponse should not be confused with the responsivity of the detector that is defined in section 3.3.2. Figures 3.8b and c clearly show response from the regions covered with graphene both in DC and AC at 77 Hz. The presence of photoresponse signal from regions outside the graphene area is due to lateral heat propagation in the substrate. Little or no signal is detected at the contacts as the gold reflects most of the radiation and thus no significant heating of the substrate occurs.

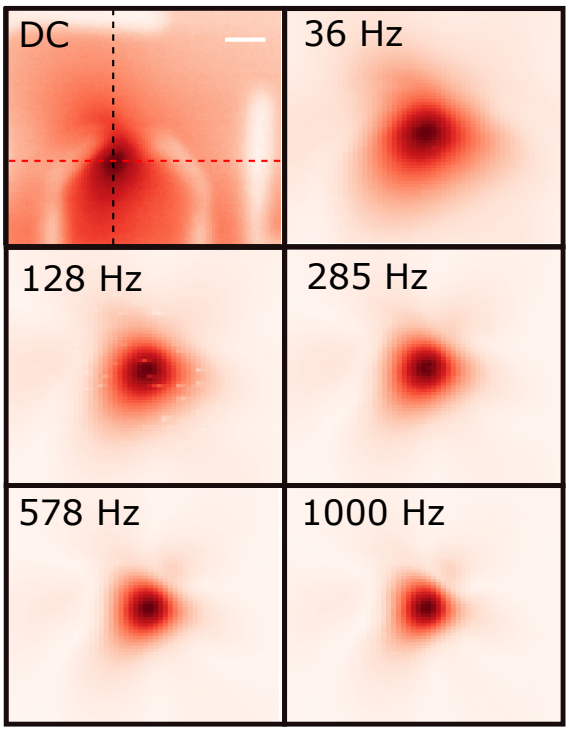

Figure 3.9: Normalized photoconductivity maps at different frequencies.Scale bar is 100 μm.

Photoresponse measured at different frequencies of the optical chopper is shown in Figure 3.9. As, expected, the area of the active region decreases as we move to higher chopper frequencies , as the lateral propagation of heat is slow.

3.3.2 Figure of Merit of the photodetector

In general, several figures of mert (FoM) are used to quantify and compare the performance of photodetectors. Responsivity, noise equivalent power (NEP) and normalized detectivity(D^*) are the most commonly used FoM for photodetectors. In this section we discuss the FoM of our pyro-resistive detector.

Responsivity

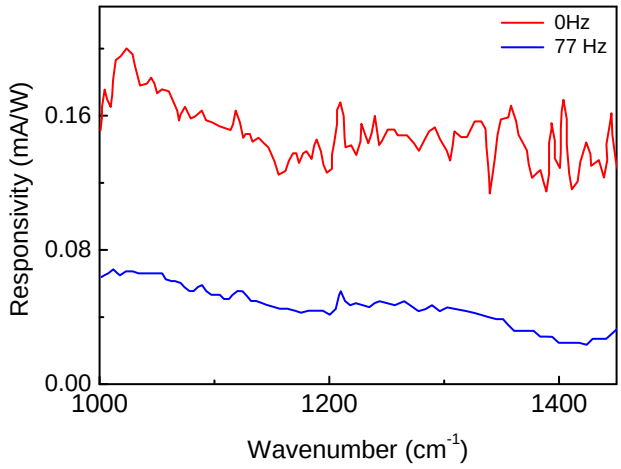

Figure 3.10: The AC (blue) and DC (red) responsivities of the photodetector as a function of the wavenumber/wavelength of excitation.

Responsivity, which is defined as the ratio of the output signal (current or voltage) to the incident radiant power is one such FoM that reflects the gain

of the detector. The responsivity R_I of the graphene/$LiNbO_3$ photodetector is dependent on the absorption of the impinging laser radiation in the substrate; as is the case with all thermal detectors. To verify such behavior we measured the photoresponse of the device in the point of maximum responsivity both in DC and at 77 Hz over the entire frequency range of the QCL (Figure 3.10). The DC measurements present higher fluctuations, mainly related to the fact that their detection is more complex while those at 77 Hz follow the wavelength absorption dependence of $LiNbO_3$.

Noise equivalent power (NEP) and Normalized detectivity (D^*)

NEP is defined as the equivalent to the radiant power that produces a signal equal to the root mean square(rms) detector noise. The detector noise is frequency dependent and often defined in terms of noise spectral density (S_n)(Figure 3.11a) so,

$$NEP = \frac{R_I}{S_n} \tag{3.4}$$

Normalized detectivity is defined as follows:

$$D^* = \frac{\sqrt{A_d B}}{NEP} = \frac{\sqrt{A_d B} R_I}{S_n} \tag{3.5}$$

The maximum D* of the device in Figure 3.8a which had an area of 75 μm$\times$75μm was 1.14$\times$10^5$cm\sqrt{Hz}$/W,(Figure 3.11b).

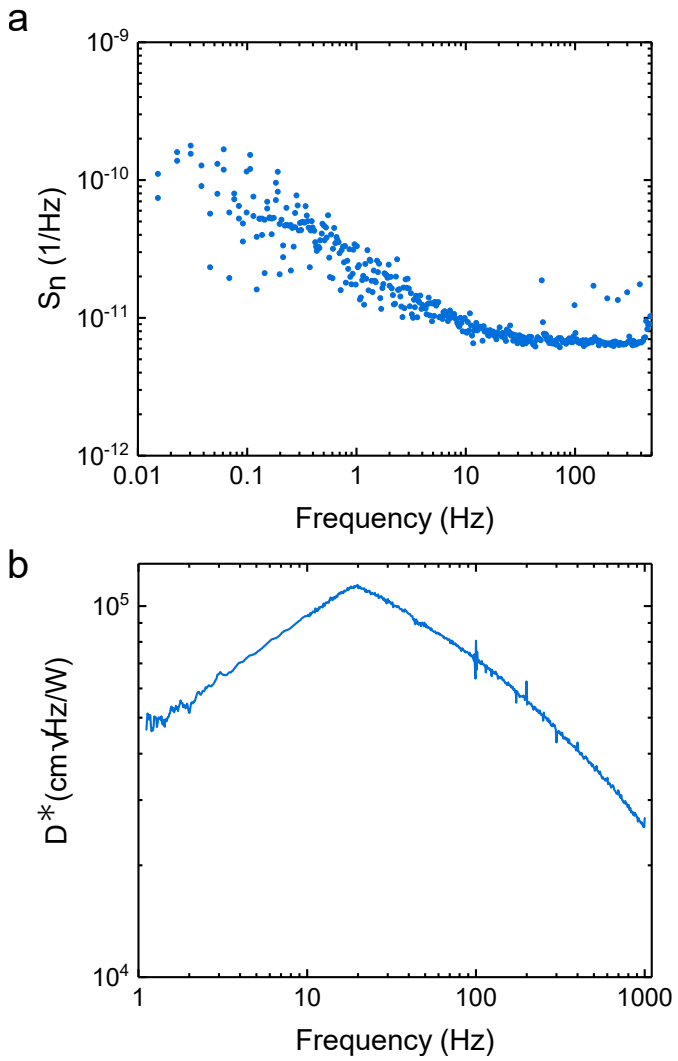

Figure 3.11: a) Frequency dependent noise spectral density of the device in Figure 3.8a. b) Normalized detectivity of the device as a function of frequency.

3.4 Model of Pyro-resistive photodetector

The pyroelectric doping effect can be described with a simple model that can also be used to optimize pyro-resistive devices. For a layer of graphene deposited on top of a z-cut $LiNbO_3$ substrate, the electrical resistance (R) change can be expressed as:

$$\frac{dR}{dP} = \frac{dR}{dq_{IND}} \frac{dq_{IND}}{dT} \frac{dT}{dP} \tag{3.6}$$

where q_{IND} is the surface pyroelectric charge and dT/dP the change in temperature induced by the incident optical power P, which depends on optical absorption and thermal conductivity of the $LiNbO_3$. This can be expanded as:

$$\frac{dR}{dP} = N_{EQ} \frac{dR_s}{dn} (\frac{dq_{IND}}{dn})^{-1} \frac{dq_{IND}}{dT} \frac{dT}{dP} \tag{3.7}$$

here, dR_s/dn is the variation of sheet resistance with respect to carrier density and depends on graphene properties such as mobility, intrinsic doping (n) and Fermi energy, $E_f = hv_f\sqrt{n\pi}$. The term dq_{IND}/dn^{-1} accounts for the number of carriers produced by each pyroelectric induced charge and depends on the density of states in graphene (typically is set to 1/e). The factor dq_{IND}/dT is proportional to the pyroelectric coefficient of the substrate. In the simplest case,we can rewrite:

$$\frac{dR}{dP} = \frac{N_{EQ}\gamma\eta_{Opt-Th}}{e} \frac{dR_s}{dn} \tag{3.8}$$

where η_{Opt-Th} accounts for the conversion efficiency from optical power to thermal power in the substrate.

Parameters of interest in performance of pyro-resistive detectors

In Equation 3.8, the term most related to graphene properties is dR_s/dn. If, for the sake of simplicity, we assume for the sheet resistance R_s a dependence with respect to n as:

$$R_s = \frac{1}{e\mu n_0} \frac{1}{\sqrt{1 + \frac{n^2}{n_0^2}}} \tag{3.9}$$

the derivative of R_s in Equation 3.9 is:

$$\frac{dR_s}{dn} = -\frac{n}{en_0^3\mu(1+\frac{n^2}{n_0^2})^{\frac{3}{2}}} \tag{3.10}$$

which has a maximum for $|n| = n_0/\sqrt{2}$. At its maximum we have:

$$\frac{dR_s}{dn}\Big|_{n=\frac{n_0}{\sqrt{2}}} = -\frac{2}{3\sqrt{3}en_0^2\mu} \tag{3.11}$$

Considering equation3.9 and the fact that max$(R_s) = 1/e\mu n_0$ we can thus assume that the maximum value of dR_s/dn is limited by the quantum of conductance such that max$(en_0\mu) = 4e^2/h$ which substituted in the previous Equation reads:

$$\frac{dR_s}{dn}\Big|_{n=\frac{n_0}{\sqrt{2}}} = -\frac{h}{2e^2n_0} \tag{3.12}$$

Within this approximation, for the best graphene samples, the intrinsic impurities density n_0 limits the responsivity. Although it is meant mainly for materials that have an exponential dependence of the resistance change with respect to temperature,a similar conclusion can be drawn if instead of the full expansion of Equation 3.8, we consider the widespread parameter of the Temperature Coefficient of Resistance (TCR). The TCR defined as $\alpha = 1/R(dR/dT)$ for pyro-resistive graphene devices is:

$$\alpha_{TCR} = \frac{1}{R_s}\frac{dR_s}{dn}\frac{dn}{dT} \tag{3.13}$$

The maximum of the TCR occurs for $n = n_0$

$$max(\alpha_{TCR}) = \frac{1}{2n_0} \tag{3.14}$$

thus further confirming the dependence of the responsivity with respect to the intrinsic impurity density of graphene.

3.4.1 Top gate tuned photoresponse of pyro-resistive graphene devices

Since, according to model in the model in Equation 3.2, the intensity of the photoresponse is expected to be dependent on the Fermi level of the graphene, measurements were taken at different graphene doping levels. The change in doping is like a bias to tune the working point of the pyro-resistive detector and was achieved by top-gating the devices.

For the top gating measurements, polyethylene oxide (PEO) was dispersed with lithium perchlorate ($LiClO_4.3H_2O$)ions (at a ratio of 2:1 approximately) in methanol,and then drop-casted on a two probe graphene device with an additional gate electrode (Figure 3.8a). Once the methanol has evaporated, the polymer acts as a solid solvent for ions (ionic gel). Ions accumulate in the vicinity of the graphene when a potential voltage is applied between the device and the external gate electrode. This allows its use as a very efficient local top gate transparent in the wavelength of interest to us. Corresponding results are shown in Figure 3.12.

Before measuring the photoresponse of the graphene device, the dependence of sheet resistance on the top-gating voltage was measured in order to extract the physical parameters of graphene. As shown in Figure 3.12a, a Lorentzian model for graphene conductivity (σ) against the top-gating voltage closely fits the experimental data with $n_0 = 7.3 \times 10^{12}$.

The photoresponse measurements performed on the devices were carried out using a coherent detection technique by chopping the laser beam at a frequency of 77 Hz and detecting the current generated by the variation of the resistance in graphene at that frequency while keeping the source-drain voltage across it constant (V_{bias}). In this case, the light impinging on the $LiNbO_3$ substrate generates an increase in temperature that is proportional to the optical power as $\Delta T = \eta_{Opt-Th} P$. The modulation of graphene carrier density produced by the pyro-electric effect, $\Delta n = \gamma_{pyro}/e\Delta T$, and the corresponding change in resistance can be written as $\Delta R = \frac{dR}{dn}\Delta n$.

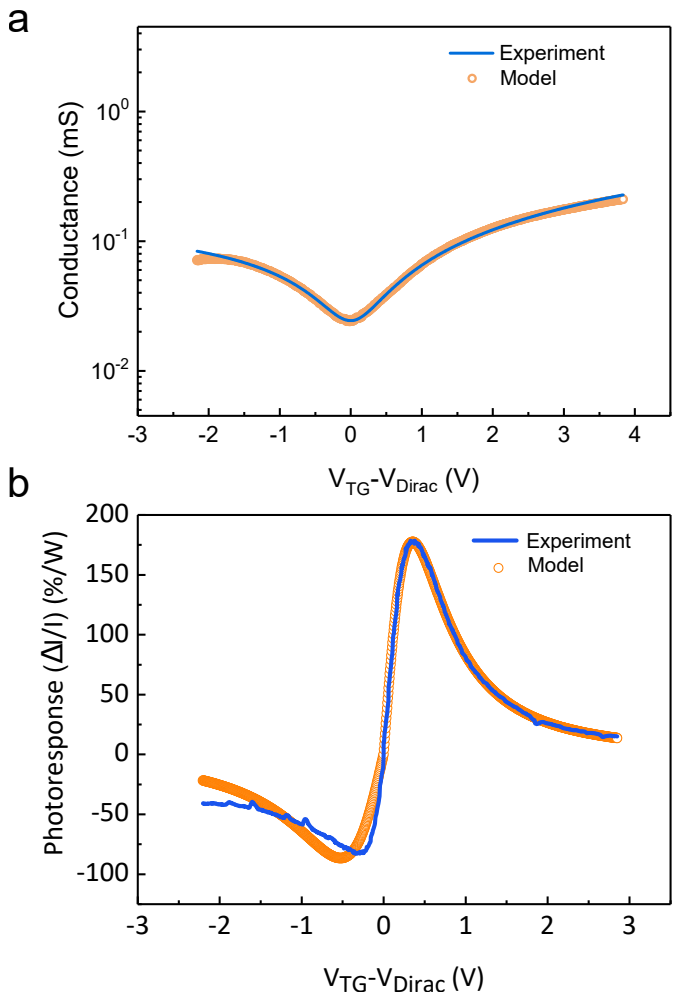

Figure 3.12: a) Conductance of graphene on $LiNbO_3$ obtained by top gating with ion gel. b)Photoresponse dependence with top gating voltage. The photoresponse defined as $\Delta I/I$ per watt follows the derivative of log σ and can be fitted as described in the text. The best fit with such function on the negative branch is not accurate,since the same Dirac curve deviates significantly from the lorentzian behavior.

Combining these expressions, we can express the modulated current produced by the light as:

$$\Delta I = \frac{V_{bias}}{R^2}\frac{dR}{dn}\frac{\gamma_{pyro}}{e}\eta_{Opt-Th}P \tag{3.15}$$

From this equation we can deduce that ΔI depends on $d\sigma$/dn and that ΔI/I depends on $dlog(\sigma)/dn$ where $\sigma = 1/R$ is the graphene conductivity. After electrical characterization, the photoresponsivity curve defined as ΔI/I versus the top-gating voltage is measured (Figure 3.12b). The curve follows the first derivative of log (σ) and the fitting is in very good agreement with the experimental results for the n-doped region. In the p-doped region the deviation from the Lorentzian shape Figure 3.12a can be attributed to the ion-gel, which is known to affect graphene mobility. Note that the deviation from the ideal behavior occurs both for resistance and photoresponse. The point of maximum photoresponsivity in Figure 3.12b, which is of interest for photodetection applications, corresponds to the flex in the Lorentzian curve of Figure 3.12b as expected from the analysis. The dependence of the photoresponsivity on the Fermi level in the proposed photodetector can be used not only to achieve the highest response by tuning the bias but also to reduce the sensitivity of the device when measuring intense light. The ability to tune the sensitivity increases its dynamic range by several orders of magnitude, this being an essential feature in many applications.

3.5 Conclusion

In conclusion, we have demonstrated that graphene in combination with $LiNbO_3$ crystal substrates can be used to make efficient photodetectors in the mid-IR based on the pyro-resistive effect, which do not require cryogenic cooling.The demonstrated detectivity compares well with some previous graphene based devices. We also detailed a model for a pyroresistive detector which can be used in the design for such detectors in the future.Although, the normalized detectivity reported for our pyro-resistive photodetector ,which is the first of its kind, is lower than the state-of-the-art detectors, this work can be seen as the

first step towards such detectors with a tunable dynamic range of operation and working at room temperature. Future developments, such as improved thermal management associated to a thinner substrate, can potentially lead to efficiency higher than current photo-detection counterparts.

Chapter 4

Ultra-thin Yttria-Stabilized Zirconia as a flexible and stable substrate for infrared nano-optics

Infrared (IR) technology is a rapidly growing field with applications ranging from thermal imaging to chemical and biological IR spectroscopy [1, 49]. Several of these applications, especially ones like spectroscopic sensing, need substrates that are transparent in the IR. Commonly used transparent substrates, such as fused silica, are transparent only up to about 2.2 μm. Instead, for longer wavelengths, calcium fluoride (CaF_2), magnesium fluoride (MgF_2), barium fluoride (BaF_2), silicon (Si), germanium (Ge) and zinc selenide (ZnSe), have been employed as substrates.The majority of these are fragile, hygroscopic or expensive. Moreover, none of them are mechanically flexible, as required by many emerging applications such as curved or bendable IR sensors [50].When mechanical flexibility is required, polymers, such as polyethylene terephthalate (PET) and polyethylene naphthalate (PEN), are used in the visible region, but their usage cannot be extended to the IR as they have several vibrational absorption

fingerprints. There exist polymers, including parylene C, polydimethylsiloxane (PDMS)and, polyimide, which are more transparent in the IR and have been studied in literature [51]. However, ultraviolet lithography is not always easy on such materials due to their sensitivity to chemicals. Figure 4.1 shows commonly used IR transparent substrates and their transmission range.

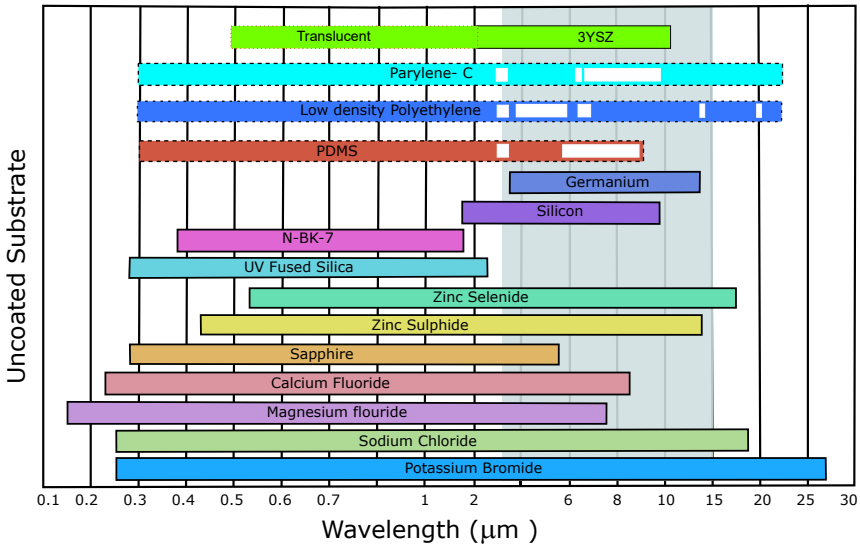

Figure 4.1: Transparency region for commonly used substrates.The grey shaded region shows the mid-IR region that is relevant in this thesis. Polymer substrates are denoted by boxes with dashed outline. The regions affected by vibrational molecular resonances are shown as white blocks in these boxes.

In addition, high-resolution electron beam lithography on these polymeric substrates is restricted by their limited thermal and radiation tolerance and non-planar nature. Alternative methods like nano-stencil lithography or self-assembly techniques could be employed to implement sub-micron features on these polymer substrates for use in plasmonic sensors [51]. Besides the difficulty in finding an appropriate lithography method for patterning, the transmission spectra of these IR polymer substrates still exhibit many vibrational fingerprints between 2-10 μm, which prevent their use in most of the near-IR (1-3 μm) and mid-IR

(3-15 μm) wavelength regions. Yttria-Stabilized Zirconia (YSZ) is a ceramic that has received a lot of attention due to its exceptional properties such as its hardness, high dielectric constant, chemical inertness and high ionic conductivity at elevated temperatures [52]. In the powder form it is used to make coatings that are chemically inert and tolerant to mechanical wear and tear, for example in cutting tools, chemical tank linings and dental restorations [53–55]. It is also used as an electrolyte in solid oxide fuel cells (SOFCs) [56]. Recently, there has been a growing interest in using thin films and micro-spheres of YSZ for various photonic applications [57,58]. For example, ENrG Inc. has commercialized 20 and 40 μm thick flexible substrates of 3 mol $\%$ YSZ (3YSZ),which has also shown remarkable transparency in the near-IR and mid-IR, while being translucent in the visible [59]. As will be described in the following sections, we have demonstrated for the first time that ultra-thin 3YSZ can be the ideal platform to implement next generation flexible IR nano-optic devices, such as plasmonic sensors and polarizers. We also show that it can be combined with graphene to make flexible transparent electrodes for the IR that can be used for cell culture spectroscopy and IR transparent shielding [60–62].

4.1 Yttria Stabilized Zirconia

Dopants such as yttria (Y_2O_3) are added to zirconia (ZrO_2) to stabilize it in its tetragonal phase at much lower temperatures than its natural existence. Such a doping of zirconia with yttria produces YSZ, in which some of the Zr^{+4} ions are substituted in the crystal lattice by the slightly larger Y^{3+} ions. YSZ has high strength and wear and fracture resistance.

Bulk YSZ ceramics are usually made by techniques such as injection molding, followed by a heat treatment to coalesce it further.The amount of Y_2O_3 added to stabilize the zirconia is varied, depending on the desired properties of the final pressed ceramic. Normally, lowering the amount of Y_2O_3 stabilizer increases fracture toughness; however, there is a trade-off with reduced mechanical strength and age resistance.

In our experiments we use 3YSZ which is known to have high strength and fracture resistance. In addition it also allows high operation temperatures and

is impermeable to both liquids and gased.

4.2 Properties of ultra-thin 3YSZ

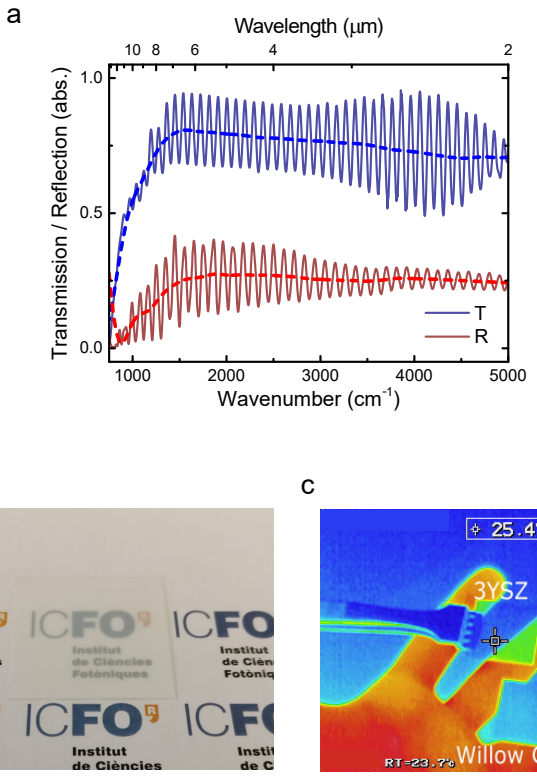

Figure 4.2: a) The Fourier Transform-Infrared Spectroscopy (FTIR) transmission (blue) and reflection (red) spectra of one-side-polished ultra-thin (20 μm-thick) 3YSZ substrate. The dashed lines show spectra taken at low resolution to avoid features from Fabry-Perot interference. b) Image of ultra-thin 3YSZ substrate that is transparent in the IR and translucent in the visible region. c) IR camera image of IR transparent 20 μm thick ultra-thin 3YSZ(top) and IR opaque 125 μm thick Corning Willow glass (bottom).

The Fourier Transform-Infrared Spectroscopy (FTIR) transmission and reflection spectra of a one-side-polished ultra-thin (20 μm-thick) 3YSZ substrate are shown in Figure 4.2a. The transmittance is more than 75% in the wavelength range from 2 to 10 μm. Note that due to a sample thickness that is comparable to mid-infrared wavelengths, the transmission and reflection spectra show features resulting from Fabry-Perot interference (continuous curve in Figure 4.2a). In the same graph, the average transmission/reflection is plotted by taking the spectra at low resolution. From Figure 4.2b we can appreciate the translucent nature of such a thin 3YSZ substrate under visible light while the IR camera image in Figure 4.2c highlights the IR transparency of the ultra-thin 3YSZ. For comparison we also show 125 μm thick Corning Willow glass which is opaque in the thermal IR range.

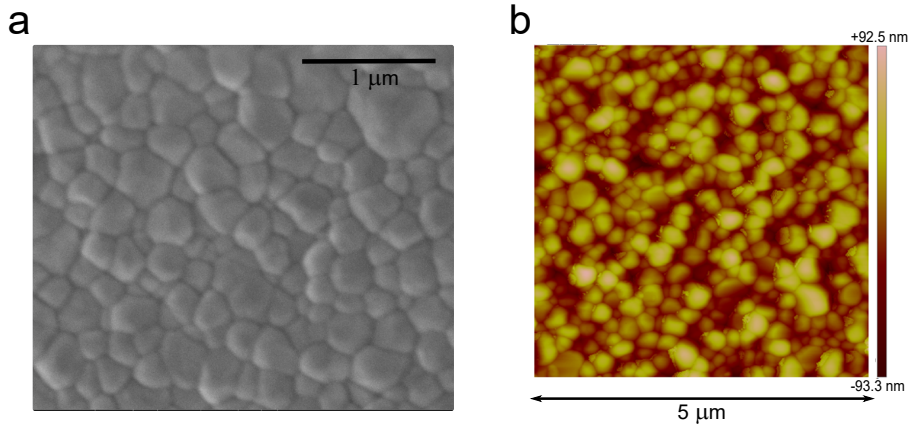

Figure 4.3: a)SEM image of the polished face of the ultra-thin (20 μm-thick) 3YSZ substrate. b)AFM image of the polished face of the ultra-thin (20 μm-thick) 3YSZ substrate.

The scanning electron microscope (SEM) image (Figure 4.3a) shows the granular structure of the surface, which is due to the fabrication technique used to make the ultra-thin-3YSZ.

The average roughness (RMS value) of the polished side of the ultra-thin-3YSZ substrate as obtained from Corning Inc. is around 20 nm (Figure 4.3b).

The level of roughness is much smaller than the IR wavelengths, so the surface scattering effects are negligible.

4.3 Flexible nano-antennas and wire-grid polarizers

4.3.1 Gold dipole antennas

In order to demonstrate the potential of the ultra-thin 3YSZ as a flexible transparent substrate in the mid-IR, we fabricated gold dipole antenna arrays which are widely used in surface enhanced infrared absorption (SEIRA) based spectroscopy as localized surface plasmon resonators [63].

Fabrication

We used double layer polymethyl methacrylate (PMMA) e-beam lithography to define dipole arrays of various dimensions. Two-layer lithography is a technique used to facilitate easier lift off in high-resolution lithography. In two-layer PMMA lithography the substrate is initially coated with a layer of PMMA with lower molecular weight (higher sensitivity) followed by another layer of PMMA with higher molecular weight (lower sensitivity). This combination of a more sensitive sublayer (bottom resist) and a less sensitive top layer (top resist) results in a neat undercut and hence easier lift off.

For the dipole antenna and the polarizer grids described in this chapter, we used a combination of AR-P 950K-679.03(top resist) and AR-P 600K-661.04 (bottom resist). The CRESTEC 50 keV electron beam lithography system was used for the exposure. After exposure and development, a 100 nm thick layer of gold (Au) with an adhesion layer of titanium (Ti) was deposited and lifted off. Unlike CaF_2 or BaF_2 substrates, ultra-thin 3YSZ shows no adhesion issues with resists and metals [64]. Fluoride substrates are also hygroscopic and cannot be used in the long term for sensors in humid or harsh environments [65]. Since the spectral range of operation is related to the antenna geometry and dimension, we fabricated gold dipole arrays of different lengths L=1.5 μm to L=2.8 μm) and periods (P=1.4L).

Figure 4.5b shows the SEM image of a typical gold dipole antenna array fabricated on the ultra-thin 3YSZ.

A Bruker FTIR Hyperion microscope (Figure 4.4) was used to measure the electromagnetic response of the antenna arrays. Measurements were performed with light polarized parallel and perpendicular to the axis of the dipoles. As expected, plasmonic modes were excited only when the incident light was polarized parallel to the axis of the dipoles.

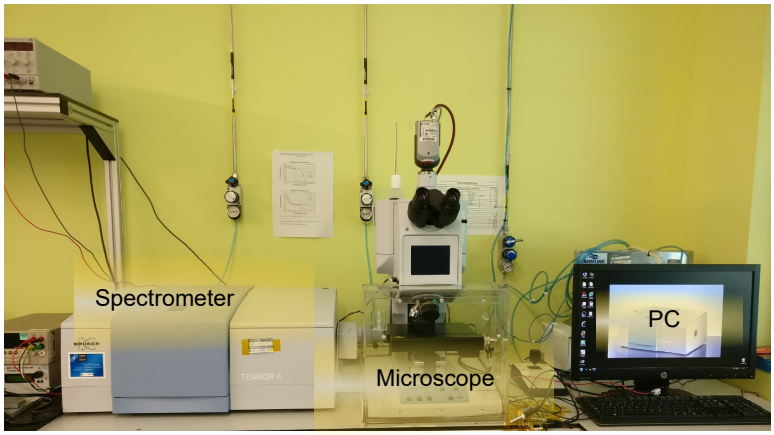

Figure 4.4: The Bruker Fourier Transform-Infrared Spectrometer (TENSOR-II) coupled to an IR microscope (HYPERION) used for the measurements.

To demonstrate mechanical flexibility, the substrate with the gold dipole arrays was fixed in between two movable aluminium rails and repeatedly bent. FTIR measurements were carried out in reflection mode while the substrate was at a bend radius, r=2.2 cm. Figure 4.5c confirms that the ultra-thin 3YSZ substrate with dipole antenna can be continuously bent without affecting the optical response.

The substrate was subjected to about 100 bending cycles and measured straight after. The difference in intensities of the plasmonic response before

and after bending was negligible, confirming the capabilities of ultra-thin 3YSZ for use as a flexible transparent substrate for IR nano-optics.

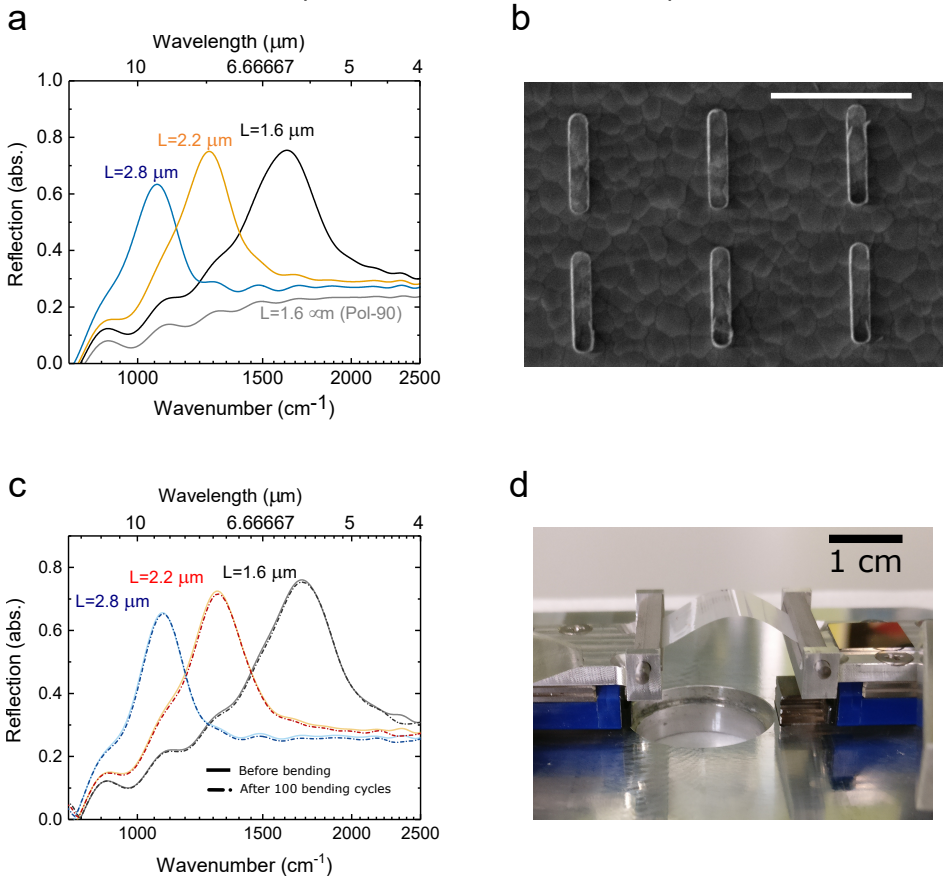

Figure 4.5: a) Reflection spectra of gold dipole arrays of different dimensions. L is the length of the dipole and the period is 1.4 L. b) SEM of one such gold dipole array. The scale bar is 2 μm. c) Reflection spectra of Au dipole arrays of three different dimensions before (solid line) and after (dot-dash line) 100 bending cycles. d) Set up used to bend the ultra-thin 3YSZ substrate with a bending radius of 2.2 cm.The scale bar is 1 cm.

4.3.2 Wire-grid polarizers

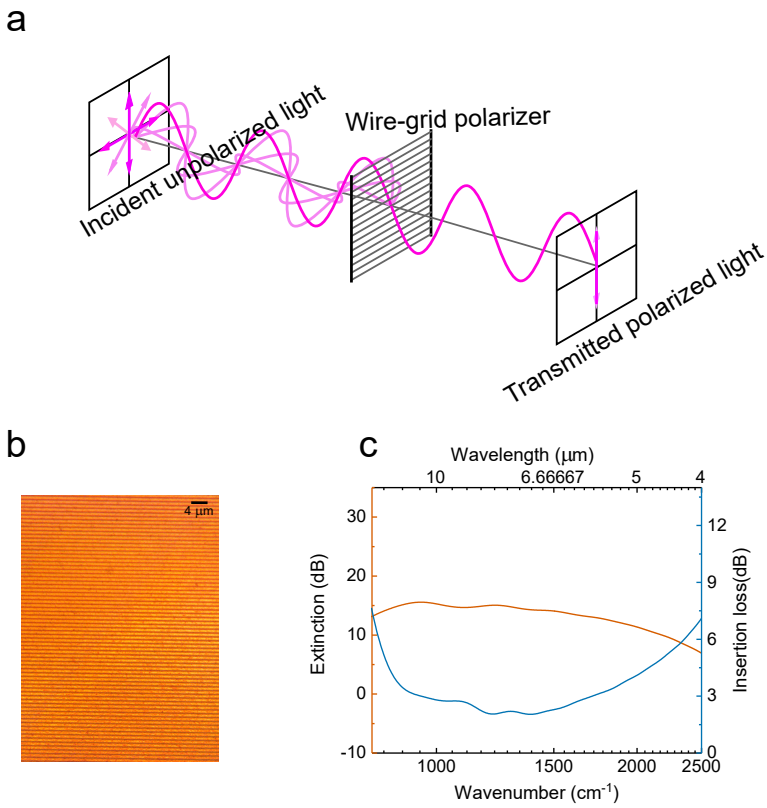

Figure 4.6: a) Schematic of a typical wire-grid polarizer. b) Optical microscope image of a wire-grid polarizer on ultra-thin 3YSZ. Scale bar is 4 μm. c) Insertion loss (maximum transmission) and extinction of a wire-grid polarizer on ultra-thin 3YSZ.

Besides their use in plasmonics (nano-optics), ultra-thin 3YSZ substrates have potential in other IR devices. For instance, polarizers are widely used devices in the mid-IR. Commercially available holographic wire-grid polarizers use materials like $BaF_2$2 , ZnSe and thallium bromoiodide (KRS-5), which can be toxic and fragile. These polarizers are also expensive due to complex fabrication tech-

niques. wire-grid polarizers consist of arrays of sub-wavelength metallic wires that transmit radiation with an electric field vector perpendicular to the wire and reflect the radiation with electric field vector parallel to the wires [66, 67]. For our experiments, we fabricated Au wire-grids with a width of 500 nm and a period of 1500 nm, for working in the 6-10 μm wavelength region. The fabrication technique was similar to the one used for the gold dipole antennas in the previous section.

The extinction of our wire-grid polarizers reaches up to 15 dB and is comparable to similar reported structures [68]. The demonstrated polarizer can potentially be used in next generation flexible IR photonic devices, for example, thermal cameras.

4.4 Graphene-based flexible IR transparent conductor and heater

Indium tin oxide (ITO) and silver nanowire (AgNW) films are known to be good transparent conductors and have been used as transparent heaters in the visible region [69, 70]. However, they both become too reflective in the IR. On the other hand, graphene is known for its high electrical conductivity and low absorption (2.3%) in the visible as well as the IR range. As ITO and AgNW has only been used in the visible range as a flexible transparent heater [71], graphene combined with the ultra-thin 3YSZ offers a unique opportunity for transparent conductors. Especially when one considers that doped graphene can have an absorption even lower than 2.3 % in the mid-IR, thanks to Pauli blocking effects [34, 72].

Here we demonstrate a transparent heater, but the same graphene on 3YSZ structure could be used for other applications, including electromagnetic (EM) shielding, plasmonics, and chemical and biological sensing.

Unlike with polymeric flexible substrates,the ultra-thin 3YSZ is planar and rigid and hence standard chemical vapor deposition (CVD) graphene transfer by wet-etching is facilitated. In addition, as it can withstand high temperatures, graphene could be grown over large areas using mass-scalable techniques, such

as CVD.

As in the previous experiments, the graphene that was initially grown on copper using CVD technique was transferred onto several ultra-thin 3YSZ substrates using PMMA as the sacrificial layer. The sheet resistance of the graphene on 3YSZ was measured to be between 1-1.5 kΩ/sq (without removing the PMMA), which is similar to the value reported on commonly used substrates like Si, SiO2 etc. [73] The corresponding Raman spectrum is shown in Figure 4.7a. The ratio between the intensities of the 2D and G peak is greater than two indicating good structural quality. After the electrical and optical characterization, we demonstrated an IR transparent flexible heater.

Figure 4.7d shows the thermal image under an electrical current. Temperatures of more than 100 °C were attained in the experiments for current densities of 1 W/cm^2. Given these performances, (shown in Figure 4.7b) the proposed IR transparent conductive structure could find applications as ATR (Attenuated Total Reflectance) component in live cell imaging, where maintaining the temperature at physiological conditions (e.g. 37 °C) as well as transparency is mandatory [62,74–76] In addition they could have great potential in EM shielding windows for detectors [77].

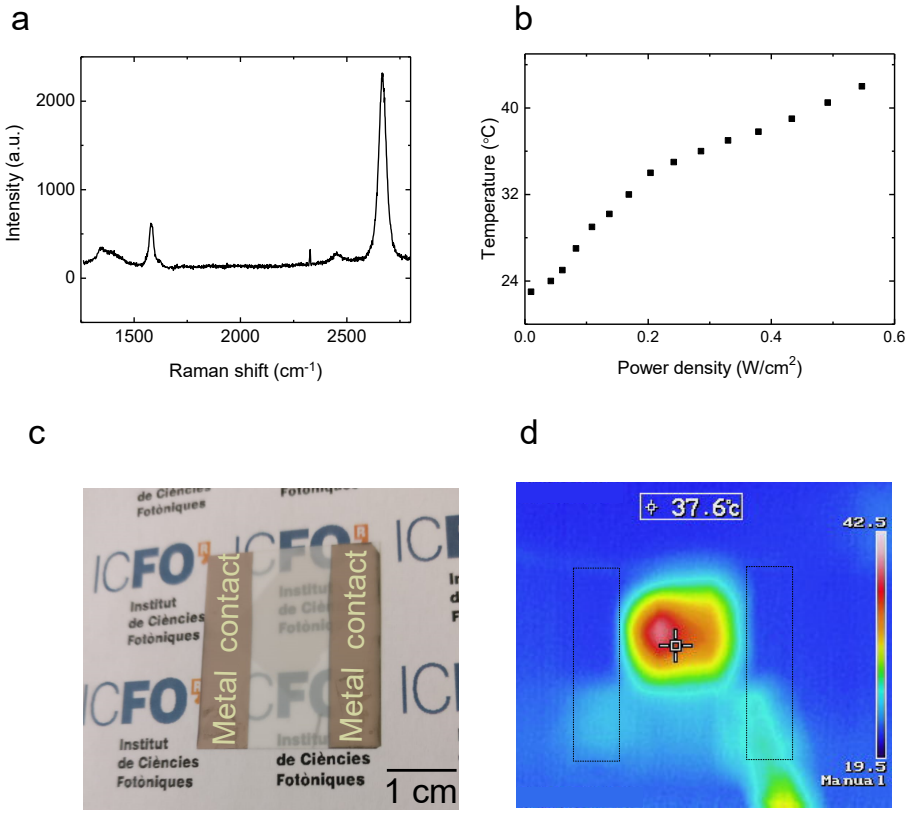

Figure 4.7: (a) Raman spectrum of graphene on ultra-thin 3YSZ. b) Temperature as a function of current through the graphene. c) Photographic image of the graphene heater. d) IR camera image of the graphene joule heater on ultra-thin 3YSZ. The gold contacts are indicated by the rectangles.

4.5 Conclusions

In conclusion, we have demonstrated that the ultra-thin 3YSZ ceramic is an ideal mechanically flexible platform to implement next generation IR nano-optic devices. In particular, we have combined YSZ with sub-wavelength metal structures and graphene to demonstrate plasmonics, polarizers and transparent heaters. The proposed ultra-thin 3YSZ based platform withstands high temperature processing, (e.g, the direct deposition of graphene), and harsh environments thanks to its high mechanical, thermal and chemical stability. In addition, besides the functional capability of making foldable and bendable devices, the mechanical flexibility of the ultra-thin 3YSZ offers the possibility of roll-to-roll processing for low cost and large-scale fabrication processes. Our work demonstrates that ultra-thin 3YSZ is a unique substrate for IR applications as it combines multiple features, including mechanical flexibility, durability, transparency, easy processing, which are not available from other available material alternatives.

Chapter 5

Scalable and tunable periodic graphene nanohole arrays for mid-infrared plasmonics

5.1 Introduction

Thanks to its unique properties like extreme sub-wavelength confinement and tunability, graphene plasmonics is relevant for many applications, including infrared detection, enhanced infrared absorption, metamaterials, chemical and bio sensing [27, 72, 78, 79]. In particular, graphene plasmonics has shown great potential in the mid-infrared (mid-IR) wavelength region, from a few to several tens of μm, where it allows, for example, highly sensitive and specific detection of molecular species via their vibrational fingerprints and photo detection of thermal radiation [80, 81].

So far, graphene plasmonics has been mainly implemented in nano-patterned graphene ribbons, disks or rings, producing localized surface plasmon resonances (LSPRs). In particular, graphene nanoribbon arrays have proven to be a robust

platform for sensing of bio-molecules in the mid-IR with high sensitivity and over an unprecedentedly wide tunable spectral range [82]. In such systems, the spectral position of the plasmonic resonance is mainly set by the lateral dimension of the graphene nanoribbons, while their spatial arrangement to form a large meta-surface allows one to obtain an exploitable plasmonic response in the far-field by adding up the contributions from thousands of uncoupled LSPR resonators. As an alternative, band engineering of graphene plasmons in a periodically patterned continuous graphene sheet has been proposed at far- infrared frequencies, analogous to photonic crystals, in so-called graphene plasmonic crystals or antidot/nanoholes arrays [83–85].

A periodic array of graphene nanoholes offers the unique feature of being an electrically connected surface, still maintaining the enhanced radiation absorption due to the excitation of graphene plasmons. It behaves both as a transparent conductive electrode and as a plasmonic absorber. Moreover, due to its simple geometry it is suitable for large-scale fabrication nano-patterning, relying, for instance, on nano-imprint or colloidal lithography [86,87]. On a more fundamental level, this platform has recently been proposed for the investigation of topologically protected plasmon modes in the infrared [88].

In this chapter, we describe the first experimental demonstration of large area, gate-tunable, graphene nanohole arrays (GNHAs) operating at mid-IR wavelengths. We demonstrate experimentally that such nanostructured graphene surfaces behave as plasmonic crystals, supporting multi-band resonances. In such nanostructures, one can tune the response by changing the geometrical parameters and/or applying an electrical voltage. Remarkably, we also show that functional, gate-tunable GNHAs can be successfully fabricated with large-scale nano-imprint lithography (NIL) over wafer-scale areas, paving the way to low-cost mid-IR plasmonic sensors.

5.2 Periodic graphene nanohole arrays

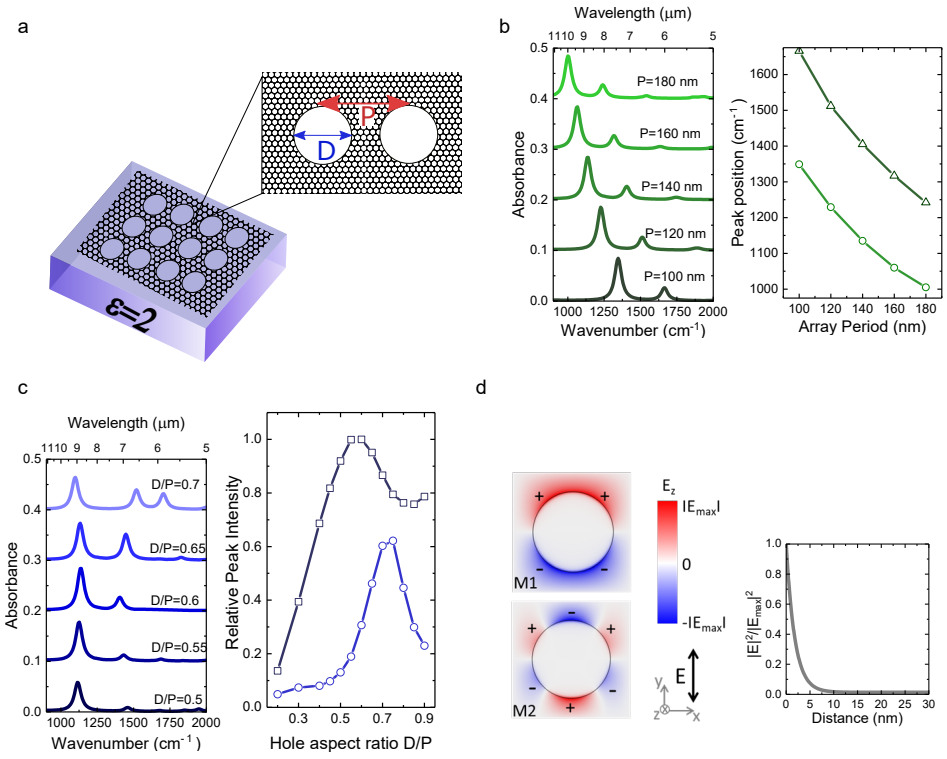

Figure 5.1: Simulations and theory of GNHAs: a) Schematic of the GNHAs/graphene plasmonic crystal, highlighting the geometric parameters P and D. b) Left: Absorption spectra for different values of array period P and a fixed aspect ratio D/P = 0.6 (E_F=0.3, τ=100 fs). The spectra are stacked for clarity. Right: Position of the the two resonance peaks as a function of the period P. c) Left: Absorption spectra for different hole aspect ratios D/P and a fixed period P=140 nm (E_F=0.3,τ =100 fs). The spectra are stacked for clarity. Right: Relative intensity of the peaks for the two visible plasmonic modes. The two modes become strongly coupled at D/P = 0.7. d) Field distribution around the GNHA.

A nanostructured surface made of graphene nanoholes of diameter D arranged in a square lattice of period P is sketched in Figure 5.1a. The photonic band structure of such a plasmonic crystal was theoretically studied by Yeung *et al.* [89]. It was found that, due to the extreme sub-wavelength confinement of the graphene plasmons, only the modes lying near the gamma point with a symmetry matching the one of the impinging light field can be excited from the far-field. We performed full-wave electromagnetic simulations using a commercial finite element package (Ansys HFSS) to study the response of the system as a function of the geometrical parameters under far-field excitation at mid-IR wavelengths.

A GNHA unit cell was simulated using periodic boundary conditions. Graphene was modeled as a two-dimensional surface with complex conductivity from the Kubo formula. The dispersion of SiO_2 was taken from Kitamura [90]. In all the simulations in Figure 5.1, the values of the graphene Fermi level and relaxation time are E_F=0.3 eV and τ =100 fs, respectively. The aim of such a study is to derive useful rules of thumb for the design of the plasmonic response for applications in the mid-IR, such as chemical sensing.

Figures 5.1b and c show the role of the two geometric parameters P and D in tailoring the optical modes of the system. In the left panel of Figure 5.1b, the simulated mid-IR absorption spectra under normal incidence for different P and fixed aspect ratio D/P=0.6 are shown. In the spectra, we observe two dominant modes whose resonant frequencies as a function of the array period are plotted in the right panel of Figure 5.1b. The spectral position of the fundamental plasmon mode corresponds to the condition where the graphene plasmon wavevector matches the first diffraction order of the array, that is $\lambda_p \approx$ P,where the plasmon effective wavelength (λ_p) is almost two orders of magnitude smaller than the free-space wavelength (typically $\lambda_p \approx \lambda_0/70$ in the mid-IR range) [78]. If we want to set the plasmon edge to around λ_0=7 μm (e.g. for chemical sensing of a specific vibrational band), then P $\approx \lambda_p \approx$ 100 nm. The effective confinement of the two modes can be inferred from the slope of the λ-P dispersion, yielding $\lambda_0/70$ for the fundamental mode (M1) and $\lambda_0/60$ for the higher order mode (M2).

In Figure 5.1c, we show the simulated absorption spectra under normal inci-

dence for different hole aspect ratio D/P and fixed period P. For the considered D/P values, we can see that the fundamental mode does not change substantially in either position or intensity whereas the visibility of M2 is greatly affected by D. The role of this parameter is better illustrated in the right panel of Figure 5.1c where the relative peak intensity for M1 and M2 (normalized to the maximum intensity of M1) is traced as a function of D/P. We focus on D/P values ranging from 0.3 to 0.7, which corresponds to dimensions compatible with the available nano-patterning methods. We can see that for increasing hole size the fundamental M1 mode grows in intensity reaching its maximum around D/P=0.6. Conversely, M2 remains almost invisible up to the value D/P=0.5 where its contrast begins to increase; for higher D/P values the two modes become coupled and a transfer of oscillator strength is produced from M1 towards M2 [85]. Eventually a situation where the two coupled plasmonic modes have similar intensity is achieved for D/P=0.65.

In summary, the periodicity P controls the spectral position of the resonances, while the nanohole diameter D mainly affects the amplitude of the resonances. It is interesting to note that this behavior is radically different from previously reported nanoribbon geometries, where the resonance frequency depends on the width W of the ribbon and is almost independent of the period P.

The out-of-plane electric field profile of the M1 and M2 modes in the far-field excitation spectra is plotted in Figure 5.1d. This figure also shows that the fundamental mode M1 is dipolar while M2 is hexapolar, such that both M1 and M2 have a non-zero dipole moment coupling with the impinging electric field. Also, the plot of the field intensity decay ($|E|^2/|E_{max}|^2$) from the graphene surface in Figure 5.1d shows that all the energy is squeezed in about 15 nm from the surface, similar to what has been reported for graphene nanoribbon arrays [80]. Hence, these graphene nanostructures are promising for surface-enhanced IR absorption (SEIRA) sensing as they combine an easy design, an extreme field confinement and the possibility to excite multiple LSPR modes, thus enabling multi-band sensing, a feature not available in nanoribbons or other localized structures.

5.3 Experimental study on GNHA

5.3.1 GNHAs using electron beam lithography

Fabrication details

A double-side polished silicon substrate with a 285 nm thin layer of native dry oxide (SiO_2) was used as the substrate. Graphene grown by chemical vapor deposition on a copper catalyst (from Graphenea Inc.) was wet-transferred to the Si/SiO_2 substrate. A 60 nm thick layer of electron beam resist was then spin coated onto the Si/SiO_2/graphene chip. Subsequently, nanohole arrays (150μm $\times$ 150 μm) with different periods and D/P ratios were exposed using the CRESTEC 50 keV electron beam lithography (EBL) system. After resist development, the nanoholes were etched with reactive ion etching using oxygen/argon plasma at 10 W for 60s. The resist was then removed using acetone, followed by isopropyl alcohol and DI water rinsing. Figure 5.2 shows the scanning electron microscope (SEM) images of different GNHA geometries.

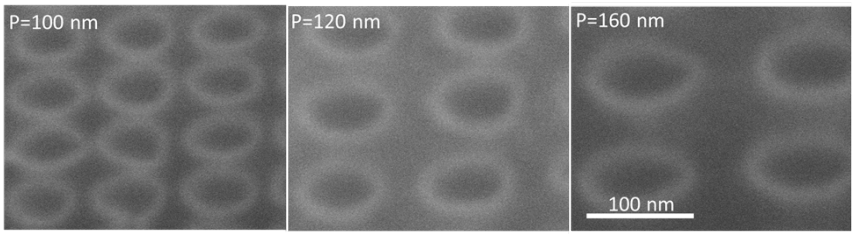

Figure 5.2: SEM images of three different GNHAs.

Plasmonic response of EBL fabricated GNHAs

The electromagnetic response of the system is quantified by the extinction spectrum measured with an infrared microscope coupled to a Fourier-transform infrared spectrometer (FTIR). The measurements were carried out in a nitrogen atmosphere to prevent atmospheric absorption lines in the spectra. The extinc-

tion spectrum is defined as 1-T/T_0, where T is the transmission through the GNHA and T_0 is the transmission spectrum of a reference area on the substrate without graphene.

Figure 5.3a shows the extinction spectra of GNHAs with different periods (100-190 nm), at a fixed D/P ratio of 0.5. Note that, unlike in graphene nanoribbon structures, the coupling of light and graphene plasmons in GNHAs is polarization independent. This is advantageous for practical applications typically using unpolarized infrared sources, as it eliminates the need for a polarizing element and the 50 $\%$ reduction of the infrared signal.

In Figure 5.3a we can see that only the fundamental plasmon mode is visible and that its position blueshifts as the period is reduced, as expected from the previous discussion. Note that the lower frequency limit of the plasmonic response achievable in our experiments is $\approx$ 1250 cm^{-1} ($\lambda \approx 8$ μm), which marks the onset of the SiO_2 Reststrahlen band (represented in grey). This substrate-related limitation can be overcome using a phonon-free mid-IR substrate (e.g. CaF_2) or changing the gate insulator (e.g. aluminum oxide or silicon nitride) [91]. The upper limit of the plasmonic response is determined in this case by the resolution of the nano-patterning technique employed and ultimately by losses associated with interband transitions. Simulated extinction spectra for the same geometric parameters are depicted in the right panel of Figure 5.3a , showing a good agreement with experimental spectra in terms of tuning range and resonance contrast.

A comparison of the experimental and simulated spectra for P=100 nm suggests that the nano-fabrication yield becomes critical for small periods affecting the quality of the plasmon response. In these simulations, E_F=0.25 eV and τ =20 fs for the graphene Fermi level and relaxation time, respectively, were found to best reproduce the inherent doping and mobility of the unbiased processed sample. These values are similar to those of previous graphene plasmonics experiments.

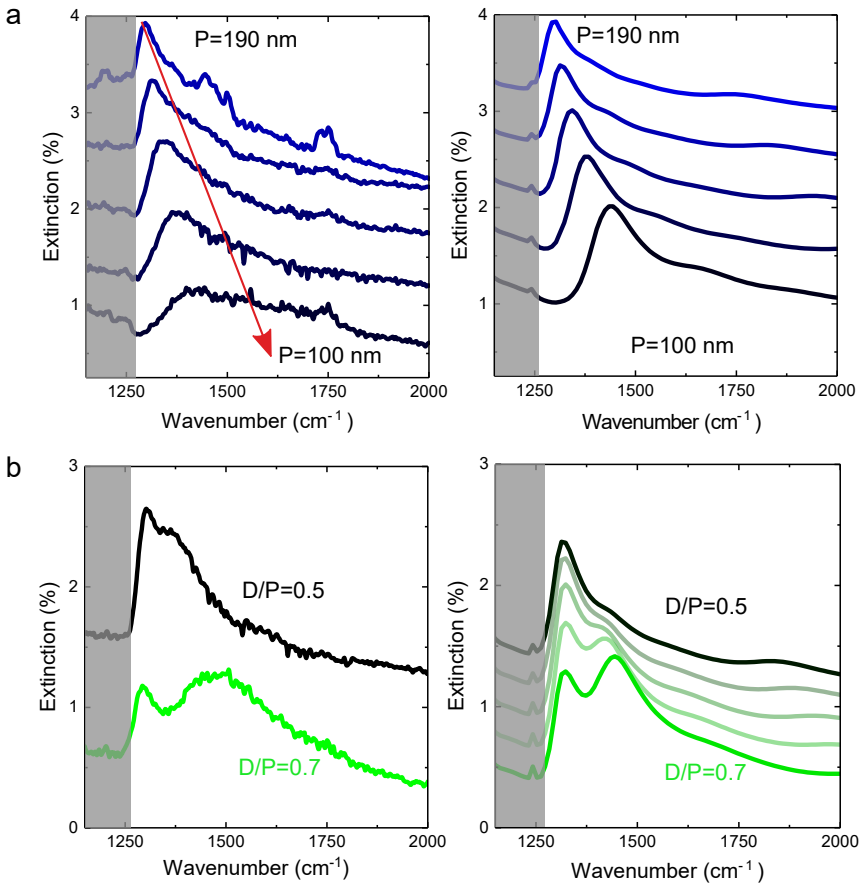

Figure 5.3: a) Experimental (left) vs simulated (right) extinction spectra for GNHAs of different periods (190, 160, 140, 120, 100 nm) and D/P=0.5. Experimental spectra are for unbiased graphene. For simulations, E_F=0.25 eV and τ=20 fs are assumed. Shadowed gray areas correspond to SiO_2 Reststrahlen bands. Curves are vertically stacked for clarity. b) Left: experimental extinction spectra for GNHAs of aspect ratio D/P=0.5 and 0.7. Right: simulated extinction spectra for GNHAs of aspect ratios from 0.5 to 0.7, showing the coupling of the two plasmonic modes. For simulations,E_F=0.3 eV and τ =20 fs is assumed. Shadowed gray areas correspond to SiO_2 Reststrahlen bands. Curves are vertically stacked for clarity.

In the left panel of Figure 5.3b, we address experimentally the role of the D/P parameter for fixed P=190 nm. We focus on two scenarios: for D/P=0.5 (black curve) only the fundamental mode M1 is clearly distinguished; for D/P=0.7 (green curve) both M1 and M2 are clearly visible and their intensities are comparable, as discussed in Figure 5.1c. The configuration where M1 and M2 are coupled is particularly relevant for applications as it allows a multi-band and broad plasmonic response in the mid-IR range relying on a very simple geometry. Obtaining the same with localized resonators (ribbons or disks) would require a complex multi-resonant geometry [82, 92, 93]. In the right panel of Figure 5.3b, the simulated extinction spectra are shown for the geometries considered in the experiment (P=190 nm, D/P=0.5 and 0.7). Additional simulations for D/P values between 0.5 and 0.7 are also shown (semi-transparent curves) to illustrate the transition between these two spectra and the coupling of M1 and M2 discussed previously. In these simulations the values E_F=0.3 eV and τ =20 fs are used to compare with the experimental data.

One of the most appealing features of graphene for mid-IR optoelectronics is the inherent tunability of its optical conductivity via electrostatic gating. In the mid-IR range this results in dynamically tunable plasmonic modes that can be exploited to devise reconfigurable optical meta-devices [94]. This fundamental feature is currently unachievable in conventional plasmonic and meta-materials based on metals and can pave the way to, for example, optical SEIRA sensors where no spectrometer is needed to achieve spectral selectivity. GNHA surfaces are extremely interesting in this sense as they can be engineered to give multiple LSPR modes in an electrically connected surface, allowing the possibility to electrostatically tune the plasmonic response without any additional contact element (as required, for instance, in graphene nanoribbons).

Figure 5.4a outlines the scheme for electrostatic tuning of the GNHA response by changing the Fermi level of graphene.

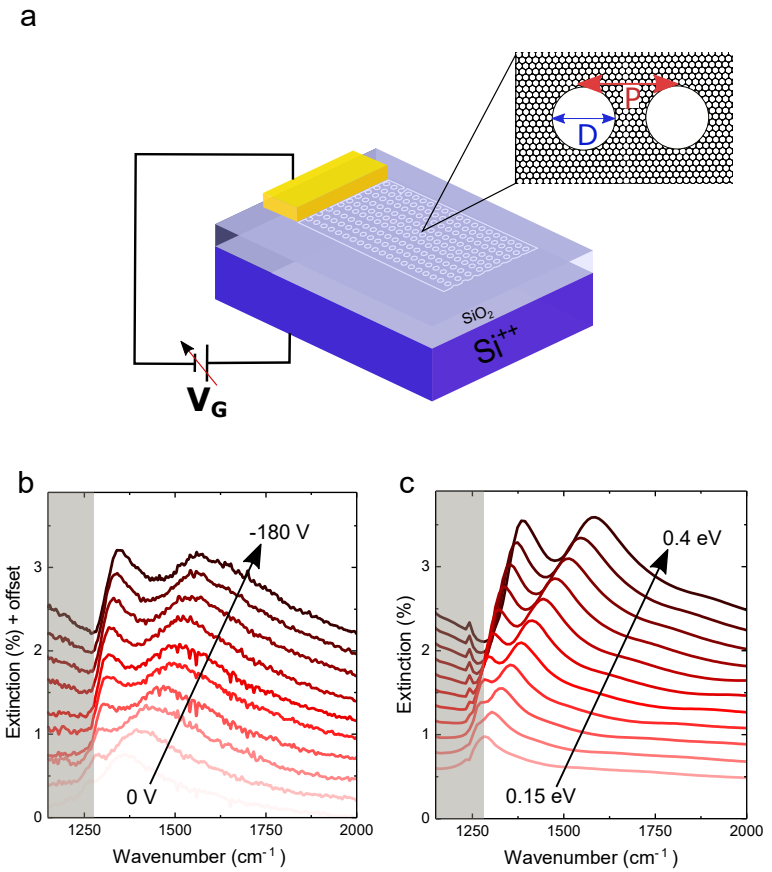

Figure 5.4: a) Schematic of electrostatic gating. b) Experimental extinction spectra as a function of the gate voltage for GNHAs with P=190 nm and D/P=0.7. Shadowed gray area corresponds to SiO_2 Reststrahlen band. Curves are vertically stacked for clarity. c) Simulated extinction spectra as a function of the Fermi energy for GNHAs with P=190 nm and D/P=0.7. Shadowed gray area corresponds to SiO_2 Reststrahlen band. Curves are vertically stacked for clarity.

Figure 5.4a shows the experimental results for the electrostatic tuning of a GNHA surface with P=180 nm and D/P =0.65 where two plasmonic bands of

similar intensity are expected. We observe a clear spectral tuning, a progressive blue shift and an increase in intensity of the plasmonic response as the bias voltage is varied from 0 to -180 V. At 0 V bias only one of the two plasmonic modes (M2) is evident due to its proximity to the SiO_2 phonon band. As the bias voltage is increased, the visibility of the fundamental mode M1 increases as it emerges from the Reststrahlen band and for high bias voltage the two become comparable. The simulated spectra as a function of the graphene Fermi level, E_F, for the same geometry are shown in Figure 5.4b and show a similar behavior corroborating the experimental results.

The GNHA samples in Figures 5.3 and 5.4 were fabricated using electron beam lithography (EBL) which is the preferred nano-patterning technique in academic research for test devices, but constitutes an unacceptable bottleneck for large scale applications due to its low throughput and high cost. A number of mass-scalable techniques have been reported in literature for large scale fabrication of graphene nanostructures, such as the block copolymer method and nanosphere lithography [95]. The latter has been used to fabricate large arrays of graphene antidots arranged in a hexagonal lattice [87]. Although excitation of plasmon-phonon modes from such graphene antidot arrays is reported, the experimental LSPR response appears poor for real applications and the electrostatic tunability of the plasmonic response has not been proven. This is attributed to large wafer-scale variations and poor reproducibility of these methods. Moreover, this method allows only a limited control of the shape and geometry of the nanostructures via the diameter and the self-assembled arrangement of the nanospheres. In fact, only a hexagonal lattice can be readily obtained from a close packed array of nanospheres without resorting to a pre-built template. Instead, the free choice of the lattice symmetry offers an important degree of freedom when engineering the response of a photonic or plasmonic crystal for a certain application [89]. Among the other scalable nano-patterning methods, nano-imprint lithography (NIL) is the most promising due to its low cost and high-throughput that satisfies industrial integration [96]. Morever, it is the best choice for large-scale periodic micro- and nanopatterns, such as plasmonic gratings or photonic crystals [97]. In the following section we describe the use of NIL in combination with laser ablation to fabricate large-area

graphene plasmonic nanostructures.

5.3.2 GNHAs using nanoimprint lithography

Fabrication details

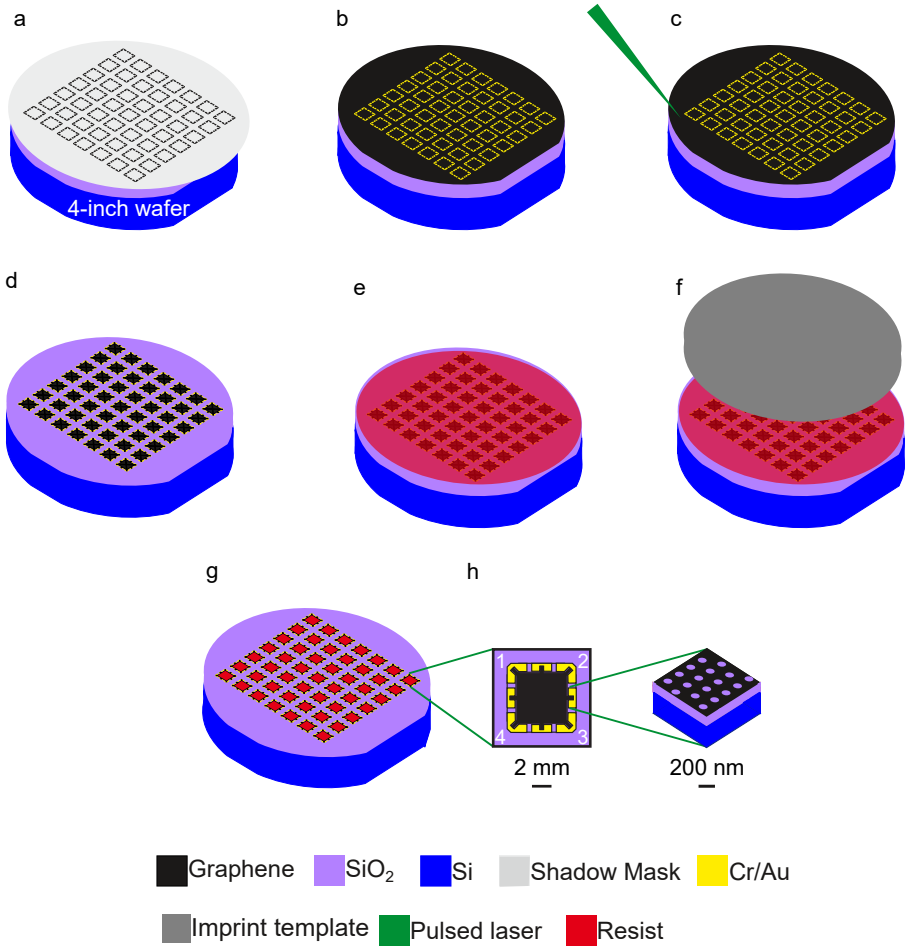

Figure 5.5: Schematic of the fabrication of GNHAs using NIL

The GNHAs using NIL described in this thesis were fabricated at Denmark Technical University (DTU) employing their fabrication technique and design guidelines provided by our group.

Graphene was grown on a commercially purchased copper foil in an Aixtron Black Magic with mm-sized single-crystal domains [98]. Prior to the graphene transfer, a double side polished silicon substrate with a 285 nm thin layer of native dry oxide (SiO_2) had metal contacts of chrome and gold (thicknesses 5 nm and 45 nm respectively) evaporated through a shadow mask. The chip size of 20 mm $\times$ 20 mm has an intended four sample areas of 5 mm $\times$ 5 mm. A large single sheet of graphene was then transferred using standard techniques [99] covering all the devices. Individual devices were then electrically separated around the perimeter of the contacts by laser ablation of unwanted graphene [100], a method that has been demonstrated not to ablate the substrate or affect the electrical properties of graphene [101]. The devices were then ready for nanoimprint lithography (NIL). The chip was spin coated with 85 nm of mr-I 7010E resist, baked at 125 °C for 60 seconds, and then thermally imprinted at 6 bar/130 °C for 10 minutes using a NILT technology CNIv2. The imprinted pattern used was the same electron-beam-lithography defined mask as presented in [10], with four 5 mm $\times$ 5 mm areas of a regular square hole pattern. The chip was then subjected to a 20 W oxygen plasma for 60 s to remove residual resist and etch the graphene. Remaining resist was removed in warm acetone and resist residuals removed by annealing at 225 °C for 30 minutes in nitrogen [102].

The total processing time after graphene transfer for laser ablation, imprint lithography and etching is less than 90 minutes. Figure 5.5 shows the schematic of the device fabrication.

Plasmonic response of NIL fabricated GNHAs

The electromagnetic response of the GNHA fabricated by NIL was measured using the Bruker FTIR in the same electrical configuration as in Figure 5.4a. Figure 5.6a shows the SEM picture of a typical GNHA fabricated by NIL.

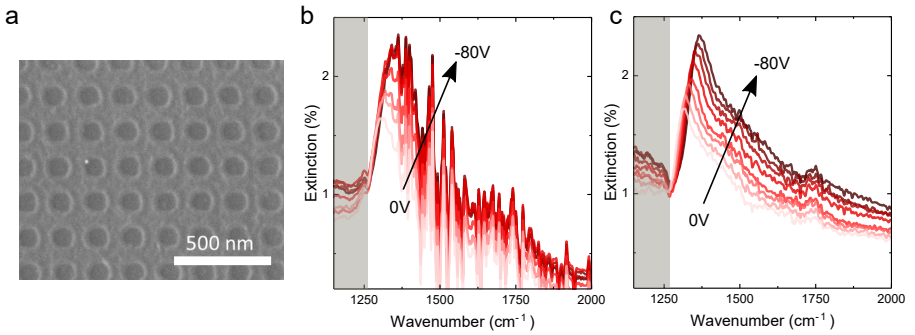

Figure 5.6: a)SEM image of GNHA fabricated by NIL. Scale bar is 500 nm b) Experimental extinction spectra as a function of the gate voltage for GNHAs fabricated with nanoimprint lithography, P=180 nm and D=110 nm. Shadowed gray area correspond to SiO_2 Reststrahlen band. The baseline of the curves have been corrected to highlight the plasmon mode tuning c) Experimental extinction spectra as a function of the gate voltage for GNHAs fabricated with e-beam lithography, P=160 nm and D=80 nm. Shadowed gray area correspond to SiO_2 Reststrahlen band.

Figures 5.6b and c depict a comparison between the extinction spectra of a GNHA fabricated with NIL and electron-beam lithography, respectively, under electrostatic tuning. Note that the spectra baselines are shown at the onset of the SiO_2 Reststrahlen band to better compare the plasmon tuning. The two surfaces have similar geometric parameters. The plasmonic responses measured are similar, in terms of both peak intensities and quality factors. However, the spectra from the NIL fabricated GNHAs are affected by the vibrational fingerprints of the polymer used in the process, which can be eliminated by annealing at high temperatures.

5.4 Conclusion

In conclusion, we have demonstrated electrostatically tunable graphene periodic nanohole arrays working in the mid-IR. In particular, we show that nanoholes arranged in a square lattice on monolayer graphene offers the possibility of

exciting multi band plasmonic resonances by properly selecting the geometric parameters. The position of these resonances can be engineered by tuning the geometrical parameters of the system. In addition, we have demonstrated that such plasmonic crystals can be fabricated by a controllable and repeatable large-scale fabrication technique on wafer-scale areas .Without such advancements, the applications of graphene plasmonics and nanostructures would be limited to the laboratory and would not progress towards industrial applications like low-cost mid-IR sensors.

Chapter 6

Summary and Outlook

This thesis is part of the extensive efforts to develop mid-IR technology and make it economically viable. In particular, novel optical surfaces using ultrathin materials, including graphene, on specific substrates for photodetection and plasmonic sensing.

In Chapter 2, we have provided a general overview of the current state and challenges faced by mid-IR technology. We also discussed some of the basic physical concepts necessary to understand the following chapters.

With the work described in Chapter 3, we developed a novel pyro-resistive photodetector based on graphene on lithium niobate ($LiNbO_3$) crystals. We exploited the high pyroelectric coefficient and absorption of $LiNbO_3$ in combination with the high doping sensitivity of graphene to achieve photodetection. Although the normalized detectivity reported for our pyro-resistive photodetector, which is the first of its kind, is lower than the state-of-the-art detectors, this work can be seen as the first step towards detectors with a tunable dynamic range of operation and working at room temperature. Our detailed model for these pyro-resistive detectors will be used as a guideline to improve the performance of such detectors in the future. With better thermal management (e.g., thinner substrates and operation in vacuum) and higher graphene quality, normalized detectivities beyond state-of-the-art photodetectors could potentially be achieved.

The work described in Chapter 4 was carried out in collaboration with Corning Inc., where we introduced, for the first time, ultra-thin 3 mol % Yttria-Stabilized Zirconia (3YSZ) as a flexible and stable substrate for nano-optic mid-IR devices. In particular, we fabricated metallic nanostructures and graphene transparent electrodes on a 3YSZ surface. These structures have allowed the demonstration of basic optical elements, including polarizers, transparent heaters and localized surface plasmonic chips. Such a 3YSZ-based platform also withstands high temperature processing and harsh environments thanks to its high mechanical, thermal and chemical stability. Moreover, the mechanical flexibility of these substrates offers the possibility of roll-to-roll processing for low cost and large-scale fabrication. We envisage that the advent of ultra-thin 3YSZ as a transparent and stable substrate will enable a new generation of bendable, low-cost and durable for mid-IR technologies.

In Chapter 5, we demonstrated for the first time tunable graphene nanostructures fabricated by a large-scale technique. In particular, we experimentally demonstrated and modelled periodic graphene nanohole surfaces and showed that they behave as plasmonic crystals, supporting multi-band resonances. In such nanostructures, one can tune the response by changing the geometrical parameters and/or applying an electrical voltage. We then demonstrated that these graphene nanohole arrays can be successfully fabricated with large-scale nano-imprint lithography (NIL), with performances similar to those obtained with expensive e-beam lithography, paving the way to low-cost mid-IR plasmonic sensors. Without such advancements, the applications of graphene plasmonics and nanostructures would be limited to the laboratory and would not progress towards industrial applications. The future applications of the large scale nanohole arrays will include demonstration of gas and bio-molecular sensing.

Bibliography

[1] Antoni. Rogalski. *Infrared detectors*. CRC Press, 2011.

[2] Frank Neubrech, Christian Huck, Ksenia Weber, Annemarie Pucci, and Harald Giessen. Surface-Enhanced Infrared Spectroscopy Using Resonant Nanoantennas. *Chemical Reviews*, 117(7):5110–5145, 4 2017.

[3] Extending opportunities. *Nature Photonics*, 6(7):407–407, 7 2012.

[4] Eustace L. Dereniak and G. D. (Glenn D.) Boreman. *Infrared detectors and systems*. Wiley, 1996.

[5] Michael A. Kinch. Fundamental physics of infrared detector materials. *Journal of Electronic Materials*, 29(6):809–817, 6 2000.

[6] Katrin Kneipp, Yang Wang, Harald Kneipp, Lev T. Perelman, Irving Itzkan, Ramachandra R. Dasari, and Michael S. Feld. Single Molecule Detection Using Surface-Enhanced Raman Scattering (SERS). *Physical Review Letters*, 78(9):1667–1670, 3 1997.

[7] Frank Neubrech, Annemarie Pucci, Thomas Walter Cornelius, Shafqat Karim, Aitzol García-Etxarri, and Javier Aizpurua. Resonant Plasmonic and Vibrational Coupling in a Tailored Nanoantenna for Infrared Detection. *Physical Review Letters*, 101(15):157403, 10 2008.

[8] Ricardo. Aroca. *Surface enhanced vibrational spectroscopy*. Wiley, 2006.

[9] Mark (Anthony Mark) Fox. *Optical properties of solids*.

[10] A. S. Barker and R. Loudon. Dielectric Properties and Optical Phonons in LiNb O 3. *Physical Review*, 158(2):433–445, 6 1967.

[11] Lukas. Novotny and Bert Hecht. *Principles of nano-optics*. Cambridge University Press, 2006.

[12] Stefan A. Maier. *Plasmonics: Fundamentals and Applications*. Springer US, New York, NY, 2007.

[13] Lukas Novotny. Effective Wavelength Scaling for Optical Antennas. *Physical Review Letters*, 98(26):266802, 6 2007.

[14] Jacob B Khurgin. How to deal with the loss in plasmonics and metamaterials. Technical report, 2015.

[15] Wen Ting Hsieh, Chieh Wu, Jacob B Khurgin, Ning Liu, and Greg Sun. Comparative Analysis of Metals and Alternative Infrared Plasmonic Materials.

[16] K S Novoselov, A K Geim, S V Morozov, D Jiang, Y Zhang, S V Dubonos, I V Grigorieva, and A A Firsov. Electric field effect in atomically thin carbon films. *Science (New York, N.Y.)*, 306(5696):666–9, 10 2004.

[17] A. K. Geim and K. S. Novoselov. The rise of graphene. *Nature Materials*, 6(3):183–191, 3 2007.

[18] K S Novoselov, A K Geim, S V Morozov, D Jiang, M I Katsnelson, I V Grigorieva, S V Dubonos, and A A Firsov. Two-dimensional gas of massless Dirac fermions in graphene. *Nature*, 438(7065):197–200, 2005.

[19] S. Das Sarma, Shaffique Adam, E. H. Hwang, and Enrico Rossi. Electronic transport in two-dimensional graphene. *Reviews of Modern Physics*, 83(2):407–470, 5 2011.

[20] R. R. Nair, P. Blake, A. N. Grigorenko, K. S. Novoselov, T. J. Booth, T. Stauber, N. M R Peres, and A. K. Geim. Fine structure constant defines visual transparency of graphene. *Science*, 320(5881):1308, 2008.

[21] Tony Low and Phaedon Avouris. Graphene Plasmonics for Terahertz to Mid-Infrared Applications. 8(2), 1086.

[22] George W Hanson. Dyadic Green's functions and guided surface waves for a surface conductivity model of graphene. *Journal of Applied Physics*, 103(6):64302, 2008.

[23] P A D Gonçalves and N M R Peres. *An Introduction to Graphene Plasmonics*. WORLD SCIENTIFIC, 6 2016.

[24] L A Falkovsky. Optical properties of graphene. *Journal of Physics: Conference Series*, 129(1):012004, 10 2008.

[25] Marinko Jablan, Hrvoje Buljan, and Marin Soljačić. Plasmonics in graphene at infrared frequencies. *Physical Review B*, 80(24):245435, 2009.

[26] Hrvoje Buljan, Marinko Jablan, and Marin Soljačić. Graphene plasmonics: Damping of plasmons in graphene. *Nature Photonics*, 7(5):346–348, 2013.

[27] Long Ju, Baisong Geng, Jason Horng, Caglar Girit, Michael Martin, Zhao Hao, Hans A Bechtel, Xiaogan Liang, Alex Zettl, Y Ron Shen, and Feng Wang. Graphene plasmonics for tunable terahertz metamaterials. *Nature Nanotechnology*, 6(10):630–634, 2011.

[28] Dafei Jin, Anshuman Kumar, Kin Hung Fung, Jun Xu, and Nicholas X Fang. Terahertz plasmonics in ferroelectric-gated graphene. *Applied Physics Letters*, 102(20):201118, 2013.

[29] Kwan Chi. Kao. *Dielectric Phenomena in Solids*. Elsevier, 2004.

[30] R W Whatmore. Pyroelectric devices and materials. *Reports on Progress in Physics*, 49(12):1335–1386, 1986.

[31] Paul Muralt. Micromachined infrared detectors based on pyroelectric thin films. *Reports on Progress in Physics*, 64(10):1339–1388, 2001.

[32] Thomas Mueller, Fengnian Xia, and Phaedon Avouris. Graphene photodetectors for high-speed optical communications. *Nature Photonics*, 4(5):297–301, 2010.

[33] Gerasimos Konstantatos, Michela Badioli, Louis Gaudreau, Johann Osmond, Maria Bernechea, F Pelayo Garcia de Arquer, Fabio Gatti, and Frank H L Koppens. Hybrid graphene–quantum dot phototransistors with ultrahigh gain. *Nature Nanotechnology*, 7(6):363–368, 2012.

[34] F Bonaccorso, Z Sun, T Hasan, and A C Ferrari. Graphene photonics and optoelectronics. *Nature Photonics*, 4(9):611–622, 2010.

[35] M Badioli, A Woessner, K J Tielrooij, S Nanot, G Navickaite, T Stauber, F J de Abajo, and F H L Koppens. Phonon-Mediated Mid-Infrared Photoresponse of Graphene. *Nano Letters*, 14(11):6374–6381, 2014.

[36] Allen L Hsu, Patrick K Herring, Nathaniel M Gabor, Sungjae Ha, Yong Cheol Shin, Yi Song, Matthew Chin, Madan Dubey, Anantha P Chandrakasan, Jing Kong, Pablo Jarillo-Herrero, and Tomás Palacios. Graphene-Based Thermopile for Thermal Imaging Applications. *Nano Letters*, 15(11):7211–7216, 2015.

[37] S Y Zhou, G.-H. Gweon, A V Fedorov, P N First, W A de Heer, D.-H. Lee, F Guinea, A H Castro Neto, and A Lanzara. Substrate-induced bandgap opening in epitaxial graphene. *Nature Materials*, 6(10):770–775, 2007.

[38] Jian-Hao Chen, Chaun Jang, Shudong Xiao, Masa Ishigami, and Michael S Fuhrer. Intrinsic and extrinsic performance limits of graphene devices on SiO2. *Nature Nanotechnology*, 3(4):206–209, 2008.

[39] Emil B Song, Bob Lian, Sung Min Kim, Sejoon Lee, Tien-Kan Chung, Minsheng Wang, Caifu Zeng, Guangyu Xu, Kin Wong, Yi Zhou, Haider I Rasool, David H Seo, Hyun-Jong Chung, Jinseong Heo, Sunae Seo, and Kang L Wang. Robust bi-stable memory operation in single-layer graphene ferroelectric memory. *Applied Physics Letters*, 99(4):42109, 2011.

[40] Guang-Xin Ni, Yi Zheng, Sukang Bae, Chin Yaw Tan, Orhan Kahya, Jing Wu, Byung Hee Hong, Kui Yao, and Barbaros Özyilmaz. Graphene–Ferroelectric Hybrid Structure for Flexible Transparent Electrodes. *ACS Nano*, 6(5):3935–3942, 2012.

[41] Shuying Zhen, Wang Sun, Guangze Tang, David Rooney, Kening Sun, and Xinxin Ma. Fabrication and evaluation of NiO/Y 2 O 3 -stabilized-ZrO 2 hollow fibers for anode-supported micro-tubular solid oxide fuel cells. *Ceramics International*, 42(7):8559–8564, 2016.

[42] Chun-Yi Hsieh, Yung-Ting Chen, Wei-Jyun Tan, Yang-Fang Chen, Wan Y Shih, and Wei-Heng Shih. Graphene-lead zirconate titanate optothermal field effect transistors. *Applied Physics Letters*, 100(11):113507, 2012.

[43] Eeshan Sandeep Kulkarni, Sascha Pierre Heussler, Andreas Volker Stier, Iñigo Martin-Fernandez, Henrik Andersen, Chee-Tat Toh, and Barbaros Özyilmaz. Exploiting the IR Transparency of Graphene for Fast Pyroelectric Infrared Detection. *Advanced Optical Materials*, 3(1):34–38, 2015.

[44] Christoph Baeumer, Diomedes Saldana-Greco, John Mark P Martirez, Andrew M Rappe, Moonsub Shim, and Lane W Martin. Ferroelectrically driven spatial carrier density modulation in graphene. *Nature Communications*, 6(1):6136, 2015.

[45] K K Wong, Institution of Electrical Engineers., and INSPEC (Information service). *Properties of lithium niobate*. INSPEC/Institution of Electrical Engineers, 2002.

[46] Simone Sanna and Wolf Gero Schmidt. Lithium niobate X-cut, Y-cut, and Z-cut surfaces from ab initio theory.

[47] Alfonso Reina, Xiaoting Jia, John Ho, Daniel Nezich, Hyungbin Son, Vladimir Bulovic, Mildred S Dresselhaus, and Jing Kong. Large Area, Few-Layer Graphene Films on Arbitrary Substrates by Chemical Vapor Deposition. *Nano Letters*, 9(1):30–35, 2009.

[48] Valerio PRUNERI, Frank KOPPENS, Davide JANNER, and Fabio GATTI. ELECTRONIC PLATFORM COMPRISING AN ABO3 TYPE CRYSTAL AND GRAPHENE, METHOD FOR ITS MANUFACTURE AND CHIP COMPRISING THE SAME. 2014.

[49] Barbara (Barbara H.) Stuart. *Infrared spectroscopy : fundamentals and applications*. J. Wiley, 2004.

[50] Juejun Hu, Lan Li, Hongtao Lin, Ping Zhang, Weidong Zhou, and Zhenqiang Ma. Flexible integrated photonics: where materials, mechanics and optics meet [Invited]. *Optical Materials Express*, 3(9):1313, 2013.

[51] Serap Aksu, Min Huang, Alp Artar, Ahmet A Yanik, Selvapraba Selvarasah, Mehmet R Dokmeci, and Hatice Altug. Flexible Plasmonics on Unconventional and Nonplanar Substrates. *Advanced Materials*, 23(38):4422–4430, 2011.

[52] George Sirinakis, Rezina Siddique, Ian Manning, Phillip H. Rogers, and Michael A. Carpenter. Development and characterization of Au-YSZ surface plasmon resonance based sensing materials: high temperature detection of CO. *The Journal of Physical Chemistry B*, 110(27):13508–13511, 2006.

[53] L B CHEN. YTTRIA-STABILIZED ZIRCONIA THERMAL BARRIER COATINGS — A REVIEW. *Surface Review and Letters*, 13(05):535–544, 2006.

[54] Zeynep Özkurt and Ender Kazazo\uglu. Zirconia Dental Implants: A Literature Review. *Journal of Oral Implantology*, 37(3):367–376, 2011.

[55] ENrG - Ceramic Technology for Clean Energy.

[56] M Ghatee, M H Shariat, and J T S Irvine. Investigation of electrical and mechanical properties of 3YSZ/8YSZ composite electrolytes. *Solid State Ionics*, 180(1):57–62, 2009.

[57] Elisabeth W. Leib, Robert M. Pasquarelli, Jefferson J. do Rosário, Pavel N. Dyachenko, Sebastian Döring, Anke Puchert, Alexander Yu. Petrov, Manfred Eich, Gerold A. Schneider, Rolf Janssen, Horst Weller, and Tobias Vossmeyer. Yttria-stabilized zirconia microspheres: novel building blocks for high-temperature photonics. *J. Mater. Chem. C*, 4(1):62–74, 2016.

[58] Guillaume Marcaud, Sylvia Matzen, Carlos Alonso-Ramos, Xavier Le Roux, Mathias Berciano, Thomas Maroutian, Guillaume Agnus, Pascal Aubert, Ludovic Largeau, Valérie Pillard, Samuel Serna, Daniel Benedikovic, Christopher Pendenque, Eric Cassan, Delphine Marris-Morini, Philippe Lecoeur, and Laurent Vivien. High-quality crystalline yttria-stabilized-zirconia thin layer for photonic applications. *Physical Review Materials*, 2(3):35202, 2018.

[59] Xin Zhao, K Jagannadham, Wuttichai Reainthippayasakul, Michael. T Lanagan, and Douglas C Hopkins. Thermal and Electrical Characterizations of Ultra-Thin Flexible 3YSZ Ceramic for Electronic Packaging Applications. *International Symposium on Microelectronics*, 2016(1):391–396, 2016.

[60] Moran M B Johnson L.F. Infrared transparent conductive oxides. *Proceedings of SPIE - The International Society for Optical Engineering*, 4375(May 2011):289–299, 2001.

[61] Z Q Li, E A Henriksen, Z Jiang, Z Hao, M C Martin, P Kim, H L Stormer, and D N Basov. Dirac charge dynamics in graphene by infrared spectroscopy. 2008.

[62] Simona Sabbatini, Carla Conti, Giulia Orilisi, and Elisabetta Giorgini. Infrared spectroscopy as a new tool for studying single living cells: Is there a niche? *Biomedical Spectroscopy and Imaging*, 6:85–99, 2017.

[63] Seong-Jun Jeong, Ju Young Kim, Bong Hoon Kim, Hyoung-Seok Moon, and Sang Ouk Kim. Directed self-assembly of block copolymers for next generation nanolithography. *Materials Today*, 16(12):468–476, 2013.

[64] L Businaro, O Limaj, V Giliberti, M Ortolani, A Di Gaspare, G Grenci, G Ciasca, A Gerardino, A de Ninno, and S Lupi. Mid-infrared nanoantenna arrays on silicon and CaF2 substrates for sensing applications. *Microelectronic Engineering*, 97:197–200, 2012.

[65] Daniel C. Harris. *Materials for Infrared Windows and Domes*. 1999.

[66] A F Kurtz, S Ramanujan, 119 XD Mi US Patent 6 665, and undefined 2003. Wire grid polarizer. *Google Patents*.

[67] S Sriram, K Steinbruegge, 638 E Supertzi US Patent 4 512, and undefined 1985. Wire grid polarizer. *Google Patents*.

[68] A Ferraro, D C Zografopoulos, M Missori, M Peccianti, R Caputo, and R Beccherelli. Flexible terahertz wire grid polarizer with high extinction ratio and low loss. *Optics Letters*, 41(9):2009, 2016.

[69] Brian G. Lewis and David C. Paine. Applications and Processing of Transparent Conducting Oxides. *MRS Bulletin*, 25(08):22–27, 8 2000.

[70] Caroline Celle, Céline Mayousse, Eléonore Moreau, Henda Basti, Alexandre Carella, and Jean-Pierre Simonato. Highly flexible transparent film heaters based on random networks of silver nanowires. *Nano Research*, 5(6):427–433, 6 2012.

[71] Daniel Schall, Muhammad Mohsin, Abhay A Sagade, Martin Otto, Bartos Chmielak, Stephan Suckow, Anna Lena Giesecke, Daniel Neumaier, and Heinrich Kurz. Infrared transparent graphene heater for silicon photonic integrated circuits. *Optics Express*, 24(8):7871, 2016.

[72] Tony Low and Phaedon Avouris. Graphene plasmonics for terahertz to mid-infrared applications, 2014.

[73] Xuesong Li, Yanwu Zhu, Weiwei Cai, Mark Borysiak, Boyang Han, David Chen, Richard D. Piner, Luigi Colombo, and Rodney S. Ruoff. Transfer of Large-Area Graphene Films for High-Performance Transparent Conductive Electrodes. *Nano Letters*, 9(12):4359–4363, 12 2009.

[74] Pedro L Fale, Ali Altharawi, and K L Andrew Chan. In situ Fourier transform infrared analysis of live cells' response to doxorubicin. *Biochimica et Biophysica Acta (BBA) - Molecular Cell Research*, 1853(10):2640–2648, 2015.

[75] Pedro L V Fale and K L Andrew Chan. Preventing damage of germanium optical material in attenuated total reflection-Fourier transform infrared (ATR-FTIR) studies of living cells. *Vibrational Spectroscopy*, 91:59–67, 2017.

[76] Hai Hu, Baoxing Liao, Xiangdong Guo, Debo Hu, Xiaofen Qiao, Ning Liu, Ruina Liu, Ke Chen, Bing Bai, Xiaoxia Yang, and Qing Dai. Large-Scale Suspended Graphene Used as a Transparent Substrate for Infrared Spectroscopy. *Small*, 13(25), 2017.

[77] Jiecai Han, Xiaona Wang, Yunfeng Qiu, Jiaqi Zhu, and Pingan Hu. Infrared-transparent films based on conductive graphene network fabrics for electromagnetic shielding. *CARBON*, 87:206–214, 2015.

[78] F Javier García De Abajo. Graphene Plasmonics: Challenges and Opportunities.

[79] A N Grigorenko, M Polini, and K S Novoselov. Optical properties of graphene. *Nature Publishing Group*, 6, 2012.

[80] Daniel Rodrigo, Odeta Limaj, Davide Janner, Dordaneh Etezadi, F. Javier García De Abajo, Valerio Pruneri, and Hatice Altug. Mid-infrared plasmonic biosensing with graphene. *Science*, 349(6244):165–168, 2015.

[81] Frank H. L. Koppens, Darrick E. Chang, and F. Javier Garcia de Abajo. Graphene Plasmonics: A Platform for Strong Light–Matter Interactions. *Nano Letters*, 11(8):3370–3377, 8 2011.

[82] Daniel Rodrigo, Tony Low, Damon B. Farmer, Hatice Altug, and Phaedon Avouris. Plasmon coupling in extended structures: Graphene superlattice nanoribbon arrays. *Physical Review B*, 93(12), 2016.

[83] Kitty Y.M. Yeung, Jingyee Chee, Hosang Yoon, Yi Song, Jing Kong, and Donhee Ham. Far-infrared graphene plasmonic crystals for plasmonic band engineering. *Nano Letters*, 14(5):2479–2484, 2014.

[84] Peter Q. Liu, Federico Valmorra, Curdin Maissen, and Jerome Faist. Electrically tunable graphene anti-dot array terahertz plasmonic crystals exhibiting multi-band resonances. *Optica*, 2(2):135, 2015.

[85] A Yu. Nikitin, F Guinea, and L Martin-Moreno. Resonant plasmonic effects in periodic graphene antidot arrays. *Applied Physics Letters*, 101(15):151119, 2012.

[86] David M.A. Mackenzie, Kristian Smistrup, Patrick R. Whelan, Birong Luo, Abhay Shivayogimath, Theodor Nielsen, Dirch H. Petersen, Sara A. Messina, and Peter Bøggild. Batch fabrication of nanopatterned graphene devices via nanoimprint lithography. *Applied Physics Letters*, 111(19), 2017.

[87] Xiaolong Zhu, Weihua Wang, Wei Yan, Martin B. Larsen, Peter Bøggild, Thomas Garm Pedersen, Sanshui Xiao, Jian Zi, and N. Asger Mortensen. Plasmon-phonon coupling in large-area graphene dot and antidot arrays fabricated by nanosphere lithography. *Nano Letters*, 14(5):2907–2913, 2014.

[88] Dafei Jin, Thomas Christensen, Marin Soljačić, Nicholas X. Fang, Ling Lu, and Xiang Zhang. Infrared Topological Plasmons in Graphene. *Physical Review Letters*, 118(24):1–6, 2017.

[89] Kitty Y.M. Yeung, Jingyee Chee, Yi Song, Jing Kong, and Donhee Ham. Symmetry Engineering of Graphene Plasmonic Crystals. *Nano Letters*, 15(8):5001–5009, 2015.

[90] Rei Kitamura, Laurent Pilon, and Miroslaw Jonasz. Optical constants of silica glass from extreme ultraviolet to far infrared at near room temperature. 46(33), 2007.

[91] Min Seok Jang, Victor W. Brar, Michelle C. Sherrott, Josue J. Lopez, Laura Kim, Seyoon Kim, Mansoo Choi, and Harry A. Atwater. Tunable large resonant absorption in a midinfrared graphene Salisbury screen. *Physical Review B - Condensed Matter and Materials Physics*, 90(16):1–5, 2014.

[92] Damon B. Farmer, Daniel Rodrigo, Tony Low, and Phaedon Avouris. Plasmon-Plasmon Hybridization and Bandwidth Enhancement in Nanostructured Graphene. *Nano Letters*, 15(4):2582–2587, 2015.

[93] Zheyu Fang, Yumin Wang, Andrea E. Schlather, Zheng Liu, Pulickel M. Ajayan, F. Javier García de Abajo, Peter Nordlander, Xing Zhu, and Naomi J. Halas. Active Tunable Absorption Enhancement with Graphene Nanodisk Arrays. *Nano Letters*, 14(1):299–304, 1 2014.

[94] Nikolay I Zheludev and Yuri S Kivshar. From metamaterials to metadevices. *Nature materials*, 11(11):917–24, 11 2012.

[95] Alberto Cagliani, David Micheal Angus Mackenzie, Lisa Katharina Tschammer, Filippo Pizzocchero, Kristoffer Almdal, and Peter Bøggild. Large-area nanopatterned graphene for ultrasensitive gas sensing. *Nano Research*, 7(5):743–754, 5 2014.

[96] Nazrin Kooy, Khairudin Mohamed, Lee Tze Pin, and Ooi Su Guan. A review of roll-to-roll nanoimprint lithography. *Nanoscale research letters*, 9(1):320, 2014.

[97] Hiroyuki Kurosawa, Bongseok Choi, Yoshimasa Sugimoto, and Masanobu Iwanaga. High-performance metasurface polarizers with extinction ratios exceeding 12000. *Optics Express*, 25(4):4446, 2017.

[98] Birong Luo, José M Caridad, Patrick R Whelan, Joachim Dahl Thomsen, David M A Mackenzie, Antonija Grubišić Čabo, Sanjoy K Mahatha, Marco Bianchi, Philip Hofmann, Peter Uhd Jepsen, Peter Bøggild, and Timothy J Booth. Sputtering an exterior metal coating on copper enclosure for large-scale growth of single-crystalline graphene. *2D Materials*, 4(4):045017, 2017.

[99] Patrick R. Whelan, Bjarke S. Jessen, Ruizhi Wang, Birong Luo, Adam C. Stoot, David M.A. Mackenzie, Philipp Braeuninger-Weimer, Alex Jouvray, Lutz Prager, Luca Camilli, Stephan Hofmann, Peter Bøggild, and Timothy J. Booth. Raman spectral indicators of catalyst decoupling for transfer of CVD grown 2D materials. *Carbon*, 117:75–81, 2017.

[100] David M.A. Mackenzie, Jonas D. Buron, Patrick R. Whelan, Bjarke S. Jessen, Adnan Silajdźić, Amaia Pesquera, Alba Centeno, Amaia Zurutuza, Peter Bøggild, and Dirch H. Petersen. Fabrication of CVD graphene-based devices via laser ablation for wafer-scale characterization. *2D Materials*, 2(4), 2015.

[101] David M.A. Mackenzie, Jonas D. Buron, Peter Bøggild, Peter U. Jepsen, and Dirch H. Petersen. Contactless graphene conductance measurements: the effect of device fabrication on terahertz time-domain spectroscopy. *International Journal of Nanotechnology*, 13(8/9):591, 2016.

[102] Lene Gammelgaard, José M. Caridad, Alberto Cagliani, David M.A. MacKenzie, Dirch H. Petersen, Timothy J. Booth, and Peter Bøggild. Graphene transport properties upon exposure to PMMA processing and heat treatments. *2D Materials*, 1(3):1–6, 2014.